Electronic Supplementary Material (ESI) for Chemical Communications.

Supporting Information for

Site-Directed Attachment of Photoexcitable Spin Labels for Light-Induced Pulsed Dipolar Spectroscopy

*Lara Williams, Sonja Tischlik, Andreas Scherer, Jörg W. A. Fischer and Malte Drescher**

Department of Chemistry and Konstanz Research School Chemical Biology, University of Konstanz, 78464 Konstanz, Germany

Table of Contents

1. LaserIMD theory

1.1 Analytical description of the LaserIMD pulse sequence

The Liouville von-Neumann (L-vN) equation $\frac{\partial \hat{\rho}}{\partial t} = -i[\widehat{H}(t), \hat{\rho}(t)]$ describes the time evolution of a density operator $\hat{\rho}(t)$. If the Hamiltonian $\widehat{H}$ is time-independent, the L-vN equation has the general solution $\hat{\rho}(t) = e^{-i\widehat{H}t}\hat{\rho}(0)e^{i\widehat{H}t}$. Presumed that the cyclic permutation relation $[\hat{A}, [\hat{A}, \hat{\rho}(0)]] = \hat{\rho}(0)$ is fulfilled (which is often the case in EPR and NMR), with $\widehat{H} = \omega\hat{A}$, it can be shown that the L-vN equation can also be solved by the expression: [1-5]

$$\hat{\rho}(0) \overset{\widehat{H}_t}{\rightarrow} \hat{\rho}(t) = \begin{cases} \hat{\rho}(0), & \text{if } [\hat{A}, \hat{\rho}(0)] = 0 \\ \cos(\omega t)\,\hat{\rho}(0) - i\sin(\omega t)[\hat{A}, \hat{\rho}(0)], & \text{if } [\hat{A}, \hat{\rho}(0)] \neq 0. \end{cases} \quad (1)$$

This so-called master equation forms the basis for the Product operator formalism (ProF).

The spin system

There are three relevant spins in the LaserIMD experiment. The spin of the permanent radical (e.g., a nitroxide) is denoted S. S is assumed to be a spin ½-system, spin systems of higher order or additional hyperfine-couplings might be possible but are ignored here. The photo label has two relevant spins, which are called L and I, they are also assumed to have a spin quantum number of ½. They form the singlet in the electronic ground state and the excited triplet (T) in the photoexcitable spin label.

The singlet ($\widehat{\boldsymbol{S}}$) and triplet ($\widehat{\boldsymbol{T}}_{+1}$, $\widehat{\boldsymbol{T}}_{0}$, $\widehat{\boldsymbol{T}}_{-1}$) density operators for the spin states of the photoexcitable spin label are[6]:

$$\widehat{\boldsymbol{S}} = \frac{1}{4}\hat{E} - \hat{L}_x\hat{I}_x - \hat{L}_y\hat{I}_y - \hat{L}_z\hat{I}_z \quad (2)$$

$$\widehat{\boldsymbol{T}}_{\boldsymbol{0}} = \frac{1}{4}\hat{E} + \hat{L}_x\hat{I}_x + \hat{L}_y\hat{I}_y - \hat{L}_z\hat{I}_z \quad (3)$$

$$\widehat{\boldsymbol{T}}_{+} = \frac{1}{4}\hat{E} + \frac{1}{2}\hat{L}_z + \frac{1}{2}\hat{I}_z + \hat{L}_z\hat{I}_z \quad (4)$$

$$\widehat{\boldsymbol{T}}_{-} = \frac{1}{4}\hat{E} - \frac{1}{2}\hat{L}_z - \frac{1}{2}\hat{I}_z + \hat{L}_z\hat{I}_z \quad (5)$$

Here, $\hat{E}$ is the identiy operator, the operators $\hat{L}_x$, etc. have their usual meaning.

The Hamiltonian

The spin Hamiltonian in its full generality has the form:

$$\hat{H} = \Omega_S \hat{S}_z + \Omega_{L/I} \hat{J}_z + \hat{\mathbf{S}}\mathbf{D}\hat{\boldsymbol{J}} + D\left(\hat{J}_z^2 - \frac{1}{3}\hat{\mathbf{J}}^2\right) + E\left(\hat{J}_x^2 - \hat{J}_y^2\right) + a\,\hat{\mathbf{J}}^2 \quad (6)$$

The spin J is the sum of the spins L and I and therefore represents the total spin of the photoexcitable spin label. $\hat{\mathbf{J}}, \hat{\mathbf{S}}, \hat{\boldsymbol{L}}$ and $\hat{\mathbf{I}}$ mean the full vector operators. The term $\Omega_S \hat{S}_z + \Omega_{L/I} \hat{J}_z$ contains the Zeeman interaction and hyperfine coupling. It will be ignored because it is refocussed by the Hahn-echo sequence of LaserIMD. The exchange interaction $a\,\hat{\mathbf{J}}^2$ separates the energies of the singlet and triplet state. As the photoexcitable spin label is either in a singlet or triplet state it can be ignored here. The term $D\left(\hat{J}_z^2 - \frac{1}{3}\hat{\mathbf{J}}^2\right) + E\left(\hat{J}_x^2 - \hat{J}_y^2\right)$ is the zero-field splitting. . The dipolar interaction $\hat{H}_\mathrm{d} = \hat{\mathbf{S}}\mathbf{D}\hat{\boldsymbol{J}}$ will be treated in the weak coupling limit: $\hat{H}_\mathrm{d} = \omega_\mathrm{d} \hat{S}_z \hat{J}_z = \omega_\mathrm{d}(\hat{S}_z \hat{L}_z + \hat{S}_z \hat{I}_z)$. In the secular approximation, the dipolar term commutes with the zero-field splitting and the zero-field splitting itself will commute with all parts in the density operator that we are going to use, so the dipolar coupling $\omega_\mathrm{d}(\hat{S}_z \hat{L}_z + \hat{S}_z \hat{I}_z)$ is the only relevant part of the Hamiltonian.

Quantum states

A photoexcited triplet has an equal population in the $|T_+>$ and $|T_->$ state[7]. As the $|T_0>$ state does not contribute to a LaserIMD signal[8], it is sufficient to assume that after the excitation, the triplet is described by a state:

$$\frac{1}{2}\hat{\boldsymbol{T}}_+ + \frac{1}{2}\hat{\boldsymbol{T}}_- = \frac{1}{4}\,\hat{E} + \hat{L}_z\,\hat{I}_z. \quad (7)$$

It can be seen that the $\hat{I}_z$- and $\hat{L}_z$- terms cancel out another, so that there is only a two-spin longitudinal magnetization ($\hat{L}_z\,\hat{I}_z$) left and there is no detectable macroscopic magnetization of the triplet state.

After the initial $\frac{\pi}{2}$ -pulse, the density-operator of the three spins S, L and I has the form: $\hat{S}_y\hat{\boldsymbol{S}}$. This corresponds to the tensor product of the spin *S* with a y-magnetization and the singlet that is formed by the spins L and I. After the photoexcitation, L and I will be in the previously described triplet state $\frac{1}{2}\,\hat{\boldsymbol{T}}_+ + \frac{1}{2}\,\hat{\boldsymbol{T}}_-$. Hence, in the overall spin state the singlet will be replaced by a triplet state: $\frac{1}{2}\hat{S}_y(\hat{\boldsymbol{T}}_+ + \hat{\boldsymbol{T}}_-)$.

Commutators

To apply the master equation, the commutators of the dipolar interaction and the spin states need to be calculated. We will do that by evaluating the commutators of the dipolar Hamiltonian ($\hat{H}_\mathrm{dd} = \omega(\,\hat{S}_z \hat{L}_z + \hat{S}_z \hat{I}_z)$) and the corresponding density operators.

We start with $\hat{S}_y\hat{\boldsymbol{S}}$.

$$[\hat{S}_z \hat{L}_z + \hat{S}_z \hat{I}_z, \hat{S}_y\hat{\boldsymbol{S}}] = [\hat{S}_z \hat{L}_z + \hat{S}_z \hat{I}_z, \hat{S}_y(\tfrac{1}{4}\hat{E} - \hat{L}_x\,\hat{I}_x - \hat{L}_y\,\hat{I}_y - \hat{L}_z\,\hat{I}_z)]$$
$$= [\hat{S}_z \hat{L}_z, \tfrac{1}{4}\hat{S}_y] + [\hat{S}_z \hat{I}_z, \tfrac{1}{4}\hat{S}_y] - [\hat{S}_z \hat{L}_z, \hat{S}_y \hat{L}_x \hat{I}_x] - [\hat{S}_z \hat{L}_z, \hat{S}_y \hat{L}_y \hat{I}_y] - [\hat{S}_z \hat{L}_z, \hat{S}_y \hat{L}_z \hat{I}_z]] - [\hat{S}_z \hat{I}_z, \hat{S}_y \hat{L}_x \hat{I}_x] -$$
$$[\hat{S}_z \hat{I}_z, \hat{S}_y \hat{L}_y \hat{I}_y] - [\hat{S}_z \hat{I}_z, \hat{S}_y \hat{L}_z \hat{I}_z]$$
$$= -\tfrac{i}{4}\hat{S}_x \hat{L}_z + \tfrac{i}{4}\hat{S}_x \hat{I}_z - \tfrac{i}{4}\hat{S}_x \hat{I}_z + \tfrac{i}{4}\hat{S}_x \hat{L}_z = 0 \quad (8)$$

This result means that there is no coupling visible if L and I form a singlet state.

Next is $\frac{1}{2}\hat{S}_y(\widehat{\boldsymbol{T}}_+ + \widehat{\boldsymbol{T}}_-)$.

$$
\begin{aligned}
&[\hat{S}_z\hat{L}_z + \hat{S}_z\hat{I}_z, \tfrac{1}{2}\hat{S}_y\,(\widehat{\boldsymbol{T}}_+ + \widehat{\boldsymbol{T}}_-)] = [\hat{S}_z\hat{L}_z + \hat{S}_z\hat{I}_z, \hat{S}_y(\tfrac{1}{4}\hat{E} + \hat{L}_z\hat{I}_z)] \\
&= \left([\hat{S}_z\hat{L}_z, \tfrac{1}{4}\hat{S}_y] + [\hat{S}_z\hat{I}_z, \tfrac{1}{4}\hat{S}_y] + [\hat{S}_z\hat{L}_z, \hat{S}_y\hat{L}_z\hat{I}_z] + [\hat{S}_z\hat{I}_z, \hat{S}_y\hat{L}_z\hat{I}_z]\right) \\
&= \left(-\tfrac{i}{4}\hat{S}_x\hat{L}_z - \tfrac{i}{4}\hat{S}_x\hat{I}_z - \tfrac{i}{4}\hat{S}_x\hat{I}_z - \tfrac{i}{4}\hat{S}_x\hat{L}_z\right) \\
&= -\tfrac{i}{2}\hat{S}_x(\hat{L}_z + \hat{I}_z) = -\tfrac{i}{2}\hat{S}_x\hat{J}_z. \qquad (9)
\end{aligned}
$$

The commutator of the dipolar coupling Hamiltonian and this operator needs to be evaluated again:

$$
\begin{aligned}
&-\tfrac{i}{2}[\hat{S}_z\hat{L}_z + \hat{S}_z\hat{I}_z, \hat{S}_x(\hat{L}_z + \hat{I}_z)] \\
&= -\tfrac{i}{2}([\hat{S}_z\hat{L}_z, \hat{S}_x\hat{L}_z] + [\hat{S}_z\hat{L}_z, \hat{S}_x\hat{I}_z] + [\hat{S}_zI_z, \hat{S}_x\hat{L}_z] + [\hat{S}_z\hat{I}_z, \hat{S}_x\hat{I}_z]) \\
&= -\tfrac{i}{2}\left(\tfrac{i}{4}\hat{S}_y + i\hat{S}_y\hat{L}_z\hat{I}_z + \tfrac{i}{4}\hat{S}_y + i\hat{S}_y\hat{L}_z\hat{I}_z\right) \\
&= \hat{S}_y(\tfrac{1}{4}\hat{E} + \hat{L}_z\hat{I}_z) = \tfrac{1}{2}\hat{S}_y\,(\widehat{\boldsymbol{T}}_+ + \widehat{\boldsymbol{T}}_-). \qquad (10)
\end{aligned}
$$

Equations (9) and (10) prove the cyclic permutation relation for the $\frac{1}{2}\hat{S}_y(\widehat{\boldsymbol{T}}_+ + \widehat{\boldsymbol{T}}_-)$ operator with the dipolar coupling Hamiltonian. Actually, the density operator of the photo-label after excitation is best described by a combination of all three triplet states. However, a similar calculation as for the singlet can be performed for the $\widehat{\boldsymbol{T}}_{\boldsymbol{0}}$ state: $[\hat{S}_z\hat{L}_z + \hat{S}_z\hat{I}_z, \hat{S}_y\widehat{\boldsymbol{T}}_0\,] = 0$. This means that the $\widehat{\boldsymbol{T}}_{\boldsymbol{0}}$ state can be ignored because no coupling is visible.

With these commutators in hand, the PRoF can be applied to LaserIMD. All pulses are assumed to be ideal with the phase x and only act on the spin S. The scenarios where the laser is before and after the π-pulse must be distinguished.

LaserIMD

The time of the laser excitation is denoted with τ, the time of the $(\pi)_x$-pulse is denoted with t_1. The echo will therefore occur at a time $2t_1$. The indices + and – will indicate the time directly before (-) or after (+) a pulse or the laser excitation

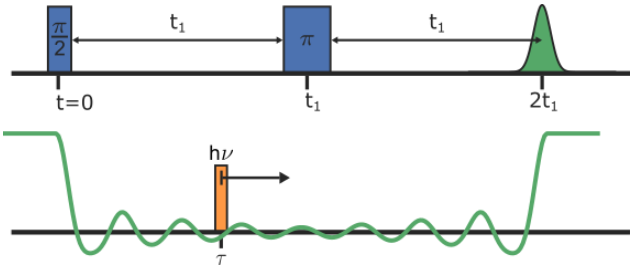

Figure S1. The LaserIMD pulse sequence.

Depending on whether the laser excitation happens before or after the π-pulse, the evolution of the density operator is described by either of these schemes:

A) Laser excitation before π-pulse:

$$\hat{\rho}(0^-) \xrightarrow{\left(\frac{\pi}{2}\right)_x} \hat{\rho}(0^+) \xrightarrow{\hat{H}_d\tau} \hat{\rho}(\tau^-) \xrightarrow{\text{laser}} \hat{\rho}(\tau^+) \xrightarrow{\hat{H}_d(t_1-\tau)} \hat{\rho}(t_1^-) \xrightarrow{(\pi)_x} \hat{\rho}(t_1^+) \xrightarrow{\hat{H}_d t_1} \hat{\rho}(2t_1) \tag{11}$$

B) Laser excitation after π-pulse:

$$\hat{\rho}(0^-) \xrightarrow{\left(\frac{\pi}{2}\right)_x} \hat{\rho}(0^+) \xrightarrow{\hat{H}_d t_1} \hat{\rho}(t_1^-) \xrightarrow{(\pi)_x} \hat{\rho}(t_1^+) \xrightarrow{\hat{H}_d(\tau-t_1)} \hat{\rho}(\tau^-) \xrightarrow{\text{laser}} \hat{\rho}(\tau^+) \xrightarrow{\hat{H}_d(2t_1-\tau)} \hat{\rho}(2t_1) \tag{12}$$

A) Laser before π-pulse

We will start with the first part (A). When the spins of the photo-label form a singlet state at the moment of the laser flash, the density operator is of the form $\rho(\tau^-) = \hat{S}_y\widehat{\boldsymbol{S}}$, as we ignore the Zeeman interaction and no coupling is visible. The laser flash excites the photoexcitable spin label from the singlet ground to the singlet excited state. Through intersystem crossing the singlet will be converted to the excited triplet state. This will eventually replace the singlet with the polarized triplet, which gives the density operator $\rho(\tau^+) = \frac{1}{2}\hat{S}_y\,(\widehat{\boldsymbol{T}}_+ + \widehat{\boldsymbol{T}}_-)$.

The system will now feel the effect of the dipolar coupling and the density operator can be written with the master equation (2) and equation (9) and (10) as:

$$\hat{\rho}(t_1^-) = \tfrac{1}{2}\cos(\omega_d(t_1-\tau))\,\hat{S}_y\left(\widehat{\boldsymbol{T}}_+ + \widehat{\boldsymbol{T}}_-\right) - \tfrac{1}{2}\sin(\omega_d(t_1-\tau))\,\hat{S}_x\hat{J}_z. \tag{13}$$

When the $(\pi)_x$-pulse comes into place, it will flip the sign of the y-magnetization from the spin S:

$$\hat{\rho}(t_1^+) = -\tfrac{1}{2}\cos(\omega_d(t_1-\tau))\,\hat{S}_y\left(\widehat{\boldsymbol{T}}_+ + \widehat{\boldsymbol{T}}_-\right) - \tfrac{1}{2}\sin(\omega_d(t_1-\tau))\,\hat{S}_x\hat{J}_z. \tag{14}$$

At the Hahn echo, the final density operator is:

$$\begin{aligned}\hat{\rho}(2t_1) = \cos(\omega_d t_1)\left(-\tfrac{1}{2}\cos(\omega_d(t_1-\tau))\,\hat{S}_y\left(\widehat{\boldsymbol{T}}_+ + \widehat{\boldsymbol{T}}_-\right) - \tfrac{1}{2}\sin(\omega_d(t_1-\tau))\,\hat{S}_x\hat{J}_z\right) + \\ \sin(\omega_d t_1)\left(\tfrac{1}{2}\cos(\omega_d(t_1-\tau))\,\hat{S}_x\hat{J}_z - \tfrac{1}{2}\sin(\omega_d(t_1-\tau))\,\hat{S}_y\left(\widehat{\boldsymbol{T}}_+ + \widehat{\boldsymbol{T}}_-\right)\right).\end{aligned} \tag{15}$$

Which simplifies to:

$$\hat{\rho}(2t_1) = -\tfrac{1}{2}\cos(\omega_\mathrm{d}\tau)\,\hat{S}_y\left(\hat{\boldsymbol{T}}_+ + \hat{\boldsymbol{T}}_-\right) - \tfrac{1}{2}\sin(\omega_\mathrm{d}\tau)\,\hat{S}_x\hat{J}_z. \tag{16}$$

Written out the density operator reads as:

$$\hat{\rho}(2t_1) = -\tfrac{1}{8}\cos(\omega_\mathrm{d}\tau)\,\hat{S}_y - \tfrac{1}{2}\cos(\omega_\mathrm{d}\tau)\,\hat{S}_y\hat{L}_z\,\hat{I}_z - \tfrac{1}{2}\sin(\omega_\mathrm{d}\tau)\,\hat{S}_x\,\hat{L}_z\hat{I}_z. \tag{17}$$

Only the first term produces detectable magnetization, which includes the expected $\cos(\omega_\mathrm{d}\tau)$ modulation.

B) Laser after π-pulse

If the laser is applied after the π-pulse, the density operator has the form $\rho(\tau^-) = -\hat{S}_y\hat{\boldsymbol{S}}$ at the moment of the laser flash. The sign is inverted with respect to the previous case because of the π-pulse that has already flipped the spins. After the laser flash, it will be $\rho(\tau^+) = -\frac{1}{2}\hat{S}_y\,(\hat{\boldsymbol{T}}_+ + \hat{\boldsymbol{T}}_-)$. Under the influence of the dipolar coupling it will evolve to:

$$\hat{\rho}(2t_1) = -\tfrac{1}{2}\cos\big(\omega_\mathrm{d}(2t_1-\tau)\big)\,\hat{S}_y\left(\hat{\boldsymbol{T}}_+ + \hat{\boldsymbol{T}}_-\right) + \tfrac{1}{2}\sin\big(\omega_\mathrm{d}(2t_1-\tau)\big)\,\hat{S}_x\hat{J}_z \tag{18}$$

$$\hat{\rho}(2t_1) = -\tfrac{1}{8}\cos\big(\omega_\mathrm{d}(2t_1-\tau)\big)\,\hat{S}_y - \tfrac{1}{2}\cos\big(\omega_\mathrm{d}(2t_1-\tau)\big)\,\hat{S}_y\hat{L}_z\,\hat{I}_z + \tfrac{1}{2}\sin\big(\omega_\mathrm{d}(2t_1-\tau)\big)\,\hat{S}_x\,\hat{L}_z\hat{I}_z. \tag{19}$$

The first term of this expression will give the $\cos(\omega_\mathrm{d}(2t_1-\tau))$-modulation of the second half of the LaserIMD curve.

Results

In summary, the combined result for the echo intensity I is:

$$I(\tau) = \begin{cases} \cos(\omega_\mathrm{d}\tau), & \text{if } \tau < t_1 \\ \cos\big(\omega_\mathrm{d}(2t_1-\tau)\big), & \text{if } \tau > t_1 \end{cases} \tag{20}$$

1.2 Theoretically achievable modulation depth

When a photoexcited triplet state is generated, the three triplet sublevels are typically not populated according to the Boltzmann distribution. Such a state, far from thermal equilibrium, is termed electron spin polarization.[9] However, the population of the three states can be quite distinct for different chromophores. Hence, the spectral shape and echo intensity of different chromophores also varies quite significantly. However, we will show here that the modulation depth that can be expected in LaserIMD does not depend on the population of the states assuming that no orientation selection is present.

Once a photo excited molecule undergoes the intersystem crossing (ISC) from the singlet to the triplet manifold, its zero field eigenstates which are denoted $|T_x>$, $|T_y>$ and $|T_z>$ will have a population that strongly depends on the exact type of the ISC.

In the presence of a high magnetic field, the above states will no longer be the eigenstates of the Hamiltonian. The relation between the zero-field eigenstates and the high-field eigenstates is presented in equations (21)-(23). We assumed here that the magnetic field is applied in the *z*-direction of the molecular frame, therefore the states $|T_{+1}>$, $|T_0>$ and $|T_{-1}>$ correspond to the molecular frame.[10, 11]

$$\left|T_x>= -\frac{1}{\sqrt{2}}\right| T_{+1}> +\frac{1}{\sqrt{2}}|T_{-1}> \tag{21}$$

$$\left|T_y>= \frac{i}{\sqrt{2}}\right| T_{+1}> +\frac{i}{\sqrt{2}}|T_{-1}> \tag{22}$$

$$|T_z> \ = |T_0> \tag{23}$$

This means that the transformation matrix that connects the zero-field basis and the high-field basis is:

$$\hat{V} = \begin{pmatrix} <T_{+1}|T_x> & <T_{+1}|T_y> & <T_{+1}|T_z> \\ <T_0|T_x> & <T_0|T_y> & <T_0|T_z> \\ <T_{-1}|T_x> & <T_{-1}|T_y> & <T_{-1}|T_z> \end{pmatrix} = \begin{pmatrix} -\frac{1}{\sqrt{2}} & \frac{i}{\sqrt{2}} & 0 \\ 0 & 0 & 1 \\ \frac{1}{\sqrt{2}} & \frac{i}{\sqrt{2}} & 0 \end{pmatrix} \tag{24}$$

The populations of the high-field eigenstates in the molecular frame can then be calculated as the diagonal elements of the density operator $\hat{\rho}_{\mathrm{mol}}$:

$$\hat{\rho}_{\mathrm{mol}} = \hat{V}\begin{pmatrix} P_x & 0 & 0 \\ 0 & P_y & 0 \\ 0 & 0 & P_z \end{pmatrix}\hat{V}^* = \begin{pmatrix} \frac{1}{2}(P_x+P_y) & 0 & \frac{1}{2}(P_y-P_x) \\ 0 & P_z & 0 \\ \frac{1}{2}(P_y-P_x) & 0 & \frac{1}{2}(P_x+P_y) \end{pmatrix} \tag{25}$$

Here, P_x, P_y and P_z are the populations of the zero-field eigenstates, the asterisk marks the adjoint matrix. In the case of a powder, the molecules have a random orientation towards the magnetic field whose orientation in the molecular frame is described by the polar angle θ and azimuthal angle ϕ. The molecular and laboratory frame are connected by a Wigner rotation matrix[12]:

$$\begin{aligned} \hat{D} &= \exp(-i\theta\hat{J}_y)\ \exp(-i\phi\hat{J}_z) \\ &= \begin{pmatrix} \frac{1+\cos(\theta)}{2}\exp -i\phi & \frac{-\sin(\theta)}{\sqrt{2}} & \frac{1-\cos(\theta)}{2}\exp i\phi \\ \frac{\sin(\theta)}{\sqrt{2}}\exp -i\phi & \cos(\theta) & \frac{-\sin(\theta)}{\sqrt{2}}\exp i\phi \\ \frac{1-\cos(\theta)}{2}\exp -i\phi & \frac{\sin(\theta)}{\sqrt{2}} & \frac{1+\cos(\theta)}{2}\exp i\phi \end{pmatrix} \end{aligned} \tag{26}$$

The density matrix can be converted to the laboratory frame according to:

$$\hat{\rho}_{\mathrm{lab}} = \hat{D}\hat{\rho}_{\mathrm{mol}}\hat{D}^{*}$$

$$= \begin{pmatrix} \frac{1+\cos(\theta)}{2}\exp -i\phi & \frac{-\sin(\theta)}{\sqrt{2}} & \frac{1-\cos(\theta)}{2}\exp i\phi \\ \frac{\sin(\theta)}{\sqrt{2}}\exp -i\phi & \cos(\theta) & \frac{-\sin(\theta)}{\sqrt{2}}\exp i\phi \\ \frac{1-\cos(\theta)}{2}\exp -i\phi & \frac{\sin(\theta)}{\sqrt{2}} & \frac{1+\cos(\theta)}{2}\exp i\phi \end{pmatrix} \begin{pmatrix} \frac{1}{2}(P_x+P_y) & 0 & \frac{1}{2}(P_y-P_x) \\ 0 & P_z & 0 \\ \frac{1}{2}(P_y-P_x) & 0 & \frac{1}{2}(P_x+P_y) \end{pmatrix} \begin{pmatrix} \frac{1+\cos(\theta)}{2}\exp i\phi & \frac{\sin(\theta)}{\sqrt{2}}\exp i\phi & \frac{1-\cos(\theta)}{2}\exp i\phi \\ \frac{-\sin(\theta)}{\sqrt{2}} & \cos(\theta) & \frac{\sin(\theta)}{\sqrt{2}} \\ \frac{1-\cos(\theta)}{2}\exp -i\phi & \frac{-\sin(\theta)}{\sqrt{2}}\exp -i\phi & \frac{1+\cos(\theta)}{2}\exp -i\phi \end{pmatrix} \quad (27)$$

As only the populations, and hence the diagonal elements, are of interest, the full density matrix is not calculated here. The resulting expressions for the high-field populations in the laboratory frame $P_{+1,\mathrm{lab}}$, $P_{0,\mathrm{lab}}$ and $P_{-1,\mathrm{lab}}$ are:

$$P_{+1,\mathrm{lab}} = \frac{P_z}{2}\sin^2\theta + \frac{P_x}{2}(\cos^2\theta + \sin^2\theta\,\sin^2\phi) + \frac{P_y}{2}(\cos^2\theta + \sin^2\theta\,\cos^2\phi) \quad (28)$$

$$P_{0,\mathrm{lab}} = P_z\cos^2\theta + P_x\sin^2\theta\,\cos^2\phi + P_y\sin^2\theta\,\sin^2\phi \quad (29)$$

$$P_{-1,\mathrm{lab}} = \frac{P_z}{2}\sin^2\theta + \frac{P_x}{2}(\cos^2\theta + \sin^2\theta\,\sin^2\phi) + \frac{P_y}{2}(\cos^2\theta + \sin^2\theta\,\cos^2\phi) \quad (30)$$

It can be seen that the population of the $|T_{+1}>$ and the $|T_{-1}>$ is always identical; hence no net magnetization from the photoexcited triplet can be expected. To get the average populations of the whole ensemble, the expressions need to be averaged over the surface of a sphere Ω.

$$<P_{+1,\mathrm{lab}}>_{\Omega} = \frac{P_z}{2}<\sin^2\theta>_{\Omega} + \frac{P_x}{2}(<\cos^2\theta + \sin^2\theta\,\sin^2\phi>_{\Omega}) + \frac{P_y}{2}(<\cos^2\theta + \sin^2\theta\,\cos^2\phi>_{\Omega}) \quad (31)$$

$$<P_{0,\mathrm{lab}}>_{\Omega} = P_z<\cos^2\theta>_{\Omega} + P_x<\sin^2\theta\,\cos^2\phi>_{\Omega} + P_y<\sin^2\theta\,\sin^2\phi>_{\Omega} \quad (32)$$

$$<P_{-1,\mathrm{lab}}>_{\Omega} = \frac{P_z}{2}<\sin^2\theta>_{\Omega} + \frac{P_x}{2}(<\cos^2\theta + \sin^2\theta\,\sin^2\phi>_{\Omega}) + \frac{P_y}{2}(<\cos^2\theta + \sin^2\theta\,\cos^2\phi>_{\Omega}) \quad (33)$$

With the help of $<\sin^2\phi>_{\Omega} = <\cos^2\phi>_{\Omega} = \frac{1}{2}$, $<\sin^2\theta>_{\Omega} = \frac{2}{3}$ and $<\cos^2\theta>_{\Omega} = \frac{1}{3}$, this gives:

$$<P_{+1,\mathrm{lab}}>_{\Omega} = \frac{1}{3}(P_x + P_y + P_z) = \frac{1}{3} \quad (34)$$

$$<P_{0,\mathrm{lab}}>_{\Omega} = \frac{1}{3}(P_x + P_y + P_z) = \frac{1}{3} \quad (35)$$

$$<P_{-1,\mathrm{lab}}>_{\Omega} = \frac{1}{3}(P_x + P_y + P_z) = \frac{1}{3} \quad (36)$$

The average population of all three states is always $\frac{1}{3}$ when averaged over the surface of a sphere and does not depend on the population of the zero-field states. As only population in the $|T_{+1}>$ and $|T_{-1}>$ state contributes to the modulation depth in LaserIMD, this means that the upper limit for the theoretically achievable modulation depth is always $\frac{2}{3}$.

2. LaserIMD simulations

The spin dynamic simulations were implemented in a home-written C++ program. The source code and all details for the simulations are available at https://github.com/andreas-scherer/LaserIMD_simulation.git. The Boost library and the Eigen library for C++ are used for the simulations. The Hamiltonian includes the Zeeman interaction of the permanent organic radical (denoted as spin A), the Zeeman interactions and zero-field splitting (ZFS) of the respective photo excitable spin label (denoted as spin B), and the dipolar coupling between them. For the LaserIMD simulations we did not include hyperfine interactions of a nitroxide for the observer spin A in order to save simulation time and we used an axial g-tensor (g_z = 2.0096 and $g_{x/y}$ = 2.0076) for the spin A for the same reason. The parameters for the simplified spin system A were chosen such that their EDFS lie on top of each other (see Figure S2).

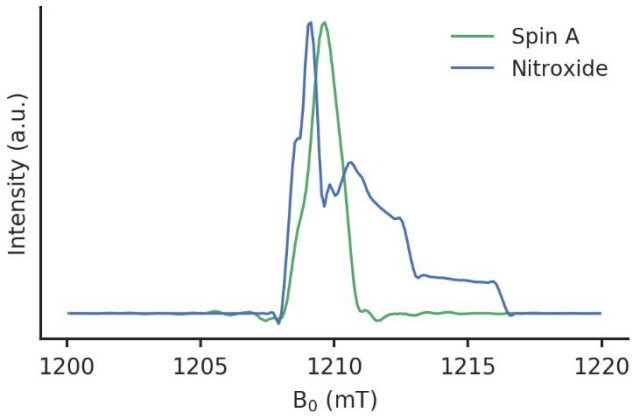

Figure S2. The simulated EDFS spectra of an exemplary MTSSL nitroxide and the EDFS spectrum that was used for the observer spin in the LaserIMD simulations. The MTSSL was simulated with g_x = 2.00906, g_z = 2.00687, and g_z = 2.00300[13] and with the hyperfine interactions A_x = 12.5 MHz, A_y = 12.5 MHz, and A_x = 97.5 MHz[14]. The EDFS of spin A was simulated with g_z = 2.0096 and $g_{x/y}$ = 2.0076. The spectra were smoothed to remove artefacts that are caused by insufficient sampling over all powder orientations.

For EO-MA, RB-MA and AT12-MA, we used the ZFS parameters and sublevel populations that were determined by the transient EPR spectroscopy experiments in this work. For the porphyrin, we used literature values.[15] For all photoexcitable spin labels we chose an isotropic g-value that was estimated from the EDFS spectra of the proteins that were labelled with a nitroxide and the respective photoexcitable spin label, where we used the nitroxide as reference. A value of g_{iso} = 2.0043 proved to be suitable. As a sanity check, we performed simulations of the EDFS spectra of the photoexcited triplet states (see Figure S3). As these simulations were perfomed in Q-band we could not directly compare them with the recorded X-band time-resolved EPR spectra in Figure S10. However, it can be seen that the main features of the time-resolved EPR spectra are reproduced correctly by the simulations.

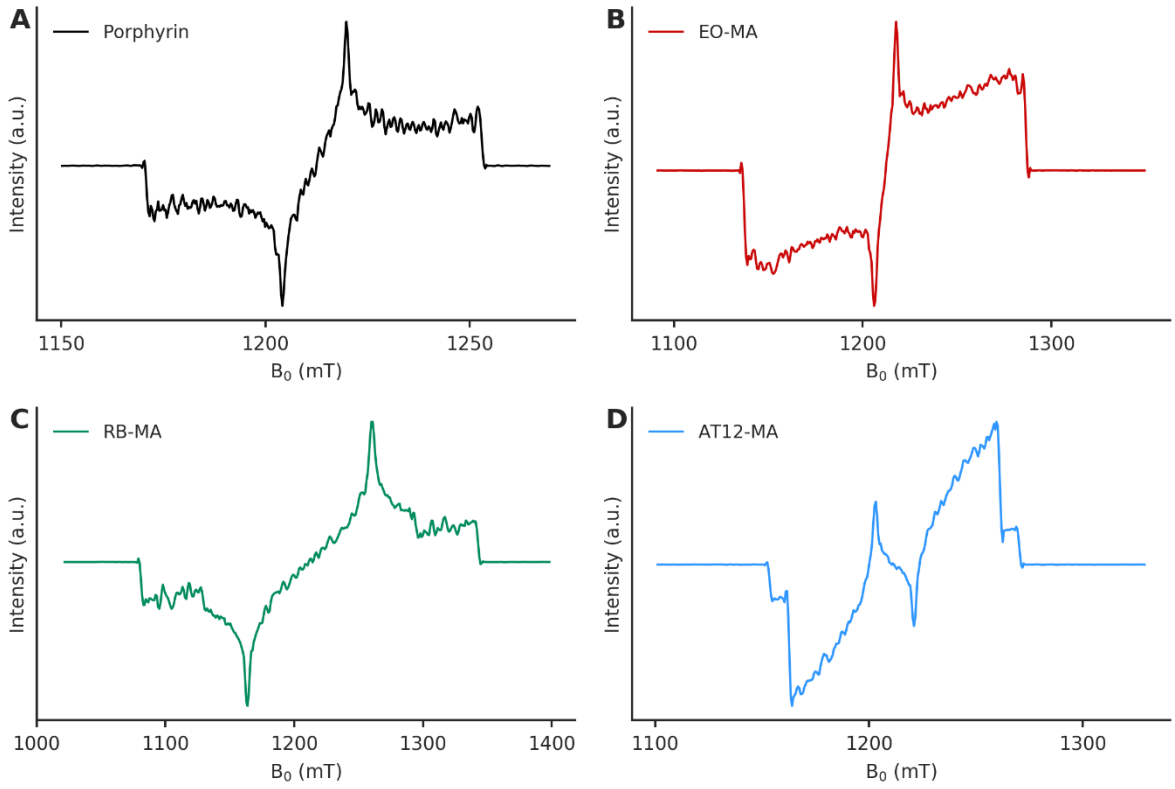

Figure S3. The simulated EDFS spectra of the photoexcitable spin labels as they were used in the LaserIMD simulations. The distortions are due to insufficient sampling over all powder orientations. For EO-MA, RB-MA and At12-MA we used the zero-field splitting values that were determined by the time-resolved EPR spectra that were recorded in this spectrum. For porphyrin we used literature values.[15]

All simulations were performed in the rotating frame approximation in Q-band (frequency: 34.00 GHz) and non-secular contributions were therefore neglected. Furthermore, the simulations do not include the phenomena relaxation, spin diffusion, and instrumental factors. The simulations perform a time-domain integration of the LvN-equation. The signal was obtained by an integration over the resulting echo. The pulses were treated as weak pulses with a π-pulse length of 24 ns.

For the LaserIMD simulations it must be considered that the spin system consists of three axis frames (the frame of spin A, spin B, and a frame for the dipolar coupling) that can rotate independent from each other. The orientation averaging was achieved by rotating every frame according to a grid that reflect its symmetry. The laser flash during the experiment was included as the Kronecker product of the density matrix $\hat{\rho}_D$ of spin A and the density matrix $\hat{\rho}_T$ of the triplet spin B:

$$\hat{\rho} = \hat{\rho}_D \otimes \hat{\rho}_T. \tag{37}$$

The populations of the triplet states were calculated according to equation (25) and (27).

3. Chemical procedures

3.1 Materials and instrumentation

All reactions were performed in flame-dried glassware under nitrogen atmosphere unless stated otherwise. Technical grade dichloromethane and ethyl acetate for column chromatography were distilled prior to use. All other solvents and reagents were purchased in the highest grade available from commercial suppliers (Sigma Aldrich, Acros, TCI) and used without further purification. Thin layer chromatography (TLC) was performed on silica gel 60 coated aluminium F254 plates (Merck) with visualisation by UV-irradiation at 254 nm and 366 nm. Flash column chromatography was carried out on silica gel 60 M, 0.04-0.083 mm mesh (Macherey Nagel) with solvent systems as specified.

^{1}H and ^{13}C NMR spectra were recorded on a Bruker Avance III 400 instrument at ambient temperature. Chemical shifts are reported relative to solvent signals ($CDCl_3$ ^{1}H, δ = 7.26 ppm, ^{13}C, δ = 77.16 ppm; methanol-d4 ^{1}H, δ = 3.31 ppm, ^{13}C, δ = 49.00 ppm; DMSO-d6 ^{1}H, δ = 2.50 ppm, ^{13}C, δ = 39.52 ppm). Preparative RP-HPLC was performed on a LC20-A prominence system (pumps LC20-AP, column oven CTO-20A, diode array detector SPD-M20A, controller CBM-20A and software LC-solution) from Shimadzu. A Nucleodur 100-5 VP C18ec column from Macherey Nagel (21 x 250 mm) was used as stationary phase and a gradient of acetonitrile in water as mobile phase. High resolution masses were measured on a micrOTOF II instrument (Bruker) in negative mode. Electrospray was used as the ionization method (ESI), and for detection the time of flight (TOF) method was applied. UV-Vis spectra were acquired on a Cary 50 Spectrophotometer (Agilent Technologies).

3.2 Synthesis

Scheme S1. Synthesis of Eosin-N_3

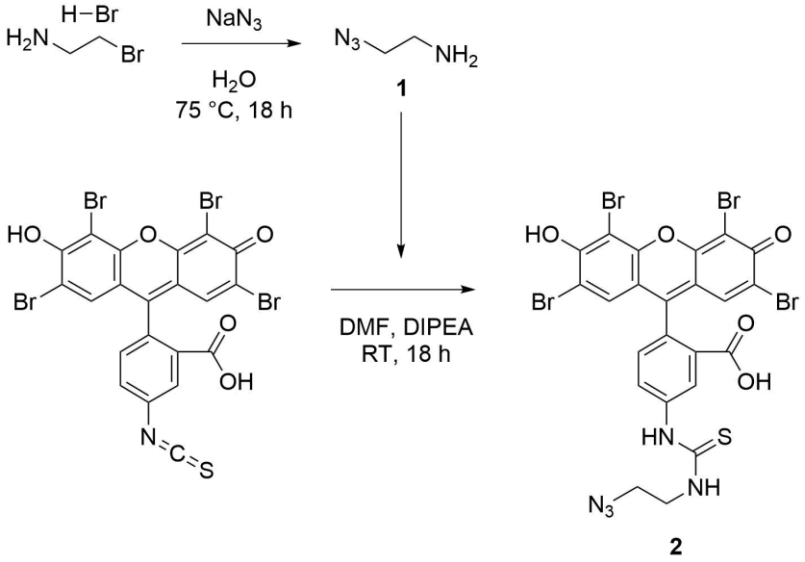

2-Aziodethylamine (1)[16]

A solution of 2-bromoethylamine hydrobromide (350 mg, 1.7 mmol, 1 equiv.) and sodium azide (333 mg, 5.1 mmol, 3 eq) in 5 mL H_2O was heated at 75 °C for 18 h. The reaction mixture was then diluted with 5 mL diethyl ether and cooled to 0 °C in an ice bath before adding solid KOH (600 mg). The organic layer was separated, and the aqueous phase extracted with diethyl ether (3 x 20 mL). The combined organic layers were dried over anhydrous $MgSO_4$ and concentrated under reduced pressure (35 °C water bath temperature, 700 mbar) to yield a clear liquid (272 mg of an ethereous solution containing 130 mg of the title compound, 1.5 mmol, 88 %).

^{1}H NMR ($CDCl_3$, 400 MHz) δ (ppm): 3.35 (t, 2H, J = 5.7 Hz), 2.87 (t, 2H, J = 5.7 Hz), 1.41 (s, 2H). **^{13}C NMR** ($CDCl_3$, 100 MHz) δ (ppm): 54.80, 41.51.

Eosin-N_3 (2)

Eosin-5-isothiocyanate (40 mg, 0.056 mmol, 1 eq) was added to a solution of **1** (14.5 mg, 0.17 mmol, 3 eq) and diisopropylethylamine (DIPEA) (30 µL, 0.168 mmol, 3 eq) in DMF (5 mL). The reaction mixture was stirred at room temperature for 18 h, then diluted with EtOAc. The organic phase was washed with 1 N HCl (3x) and brine (2x), dried over $MgSO_4$ and concentrated under reduced pressure. The residue was purified

by RP-HPLC (gradient of 60 - 100 % acetonitrile in water in 15 min) to yield **2** as an orange-red solid (23 mg, 0.03 mmol, 52 %).

^{1}H NMR (DMSO-d6, 400 MHz) δ (ppm): 10.14 (bs, 1H), 8.32 (t, 1H, J = 5.8 Hz), 8.29 (d, 1H, J = 2.3 Hz), 7.92 (d, 1H, J = 8.3 Hz), 7.38 (d, 1H, J = 8.3 Hz), 7.04 (s, 2H), 3.74 (q, 2 H, J = 5.8 Hz), 3.59 (t, 2H, J = 5.9 Hz).

^{13}C NMR (DMSO-d6, 100 MHz) δ (ppm): 180.8, 168.24, 166.3, 152.9, 151.7, 140.7, 131.6, 130.9, 129.3, 128.2, 118.4, 109.5, 99.4, 49.4, 43.1.

HRMS (ESI-TOF) m/z: calcd. for $C_{23}H_{13}Br_4N_5O_5S$ $[M-H]^-$ 785.7293, found 785.7412.

Scheme S2. Synthesis of Rose Bengal maleimide

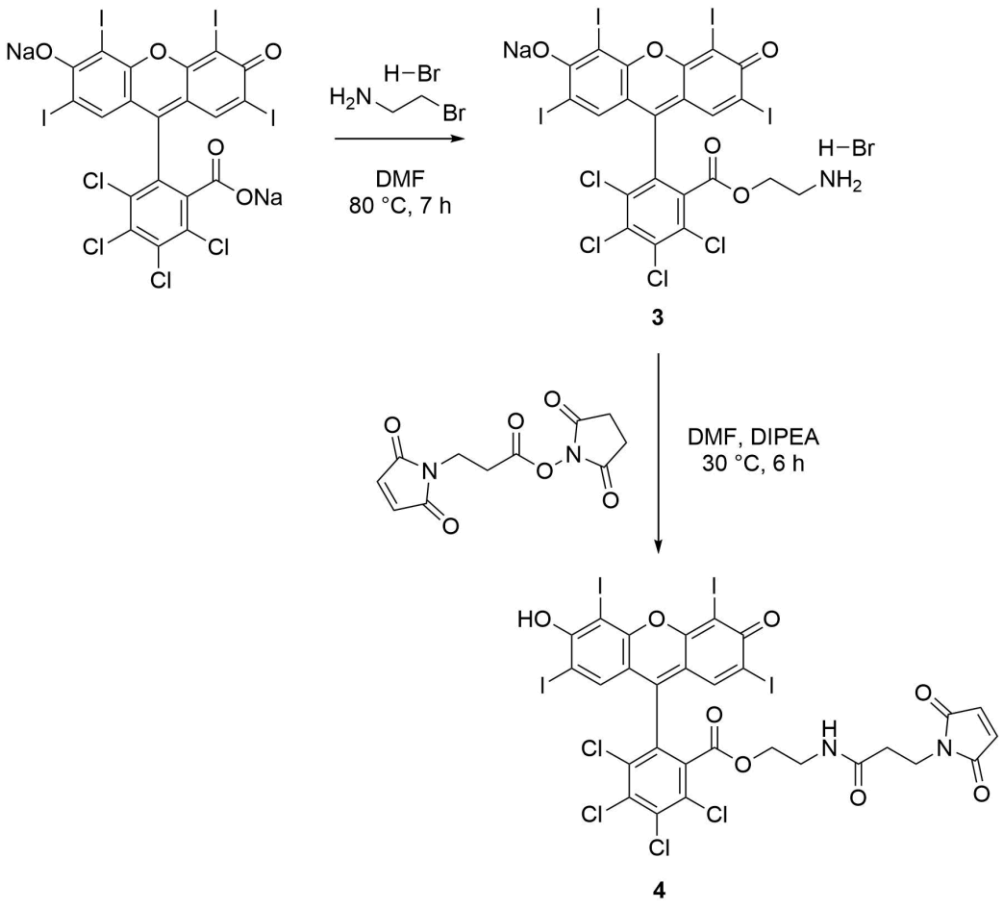

Rose Bengal amine (3)

The synthesis of **3** was derived from the method reported by C. Fowley *et al.*[17] 2-Bromoethylamine hydrobromide (50 mg, 0.24 mmol, 2.4 eq) was added to a solution of Rose Bengal disodium salt (100 mg, 0.1 mmol, 1 eq) in DMF (1.5 mL) and the mixture was stirred at 80 °C for 7 h. DMF was then removed under reduced pressure and the residue stirred in diethyl ether (20 mL) overnight. After filtration and thorough washing with diethyl ether, the residue was stirred with water (200 mL) overnight and filtered to afford a dark red solid (30 mg, 0.03 mmol, 30 %).

^{1}H NMR (DMSO-d6, 400 MHz) δ (ppm): 7.81 (bs, 3H), 7.47 (s, 2H), 4.05 (t, 2H, J = 6.3 Hz), 2.76 (t, 2H, J = 6.3 Hz).

^{13}C NMR (DMSO-d6, 100 MHz) δ (ppm): 171.8, 162.7, 157.0, 139.1, 135.9, 135.2, 134.3, 133.0, 132.0, 130.2, 129.2, 110.1, 97.4, 76.2, 62.2, 37.1.

HRMS (ESI-TOF) m/z: calcd. for $C_{22}H_8I_4Cl_4NO_5$ $[M-H]^-$ 1013.5336, found 1013.5424.

Rose Bengal maleimide (4)

Rose Bengal amine **3** (20 mg, 0.02 mmol) and DIPEA (80 µL, 0.46 mmol, 26 eq) were dissolved in DMF (5 mL). N-Succinimidyl-3-maleimidopropionate (30 mg, 0.11 mmol, 6 eq) was added in portions and the reaction stirred at 37 °C for 6 h. The reaction mixture was then diluted with EtOAc, washed with 1 N HCl (3x) and brine (2x), dried over $MgSO_4$ and concentrated under reduced pressure. The residue was purified by column chromatography (1 to 20 % MeOH in DCM) to afford **4** (15 mg, 0.017 mmol, 85 %) as a red solid.

^{1}H NMR (MeOD, 400 MHz) δ (ppm): 7.57 (s, 2H), 6.80 (s, 2H), 4.00 (t, 2H, J = 5.9 Hz), 3.72 (t, 2H, J = 6.8 Hz), 3.19 (t, 2H, J = 5.9 Hz), 2.43 (t, 2H, J = 6.8 Hz).

^{13}C NMR: (MeOD, 100 MHz) δ (ppm): 175.3, 173.2, 172.1, 164.6, 159.4, 142.9, 138.3, 136.9, 136.6, 135.5, 133.6, 131.4, 113.3, 97.0, 76.4, 65.7, 39.0, 35.8, 35.4.

HRMS (ESI-TOF) m/z: calcd. for $C_{29}H_{13}I_4N_4O_8Cl_4$ $[M-H]^-$ 1164.5605, found 1164.5707.

3.3 NMR spectra

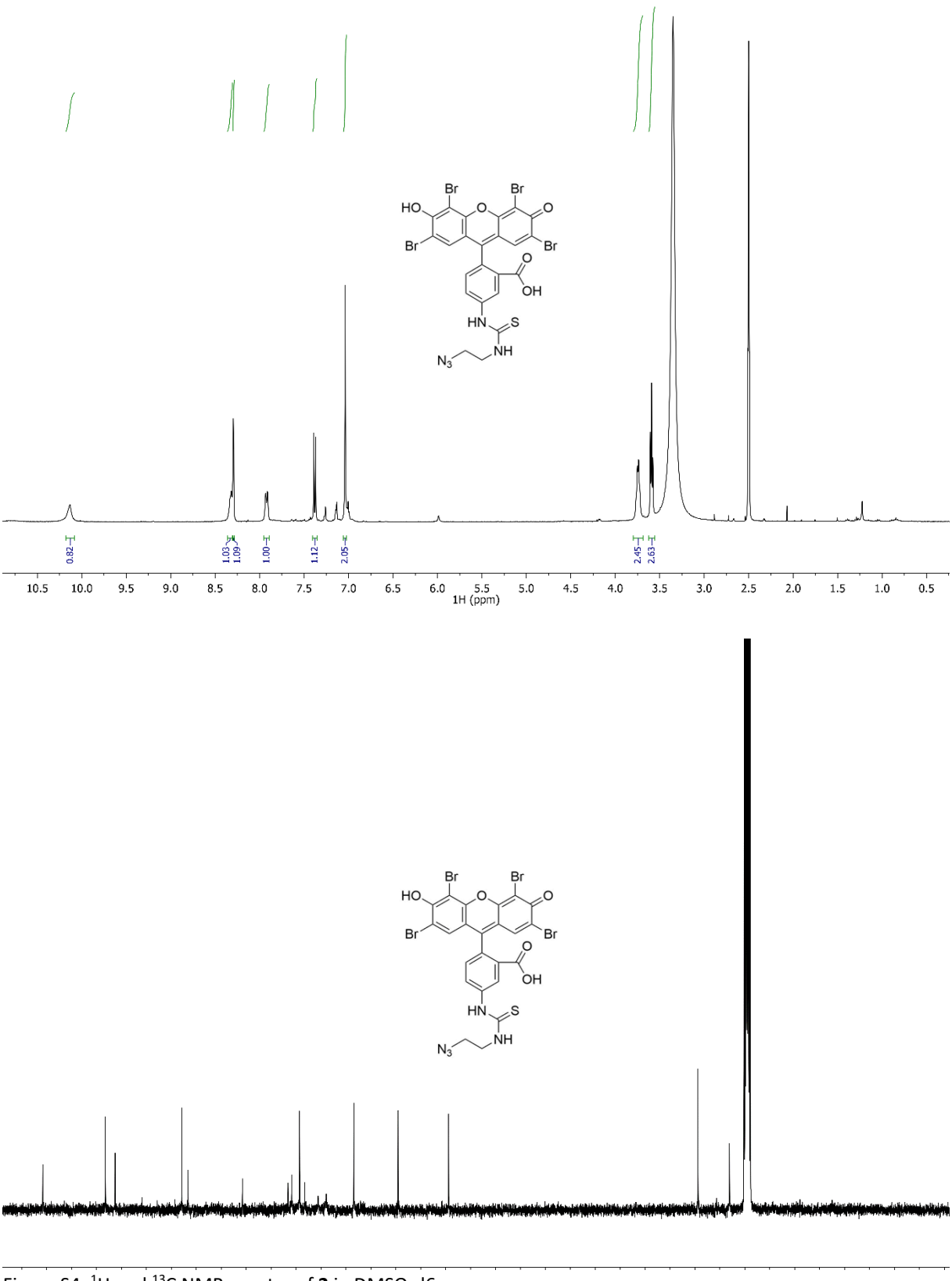

Figure S4. ^{1}H and ^{13}C NMR spectra of **2** in DMSO-d6.

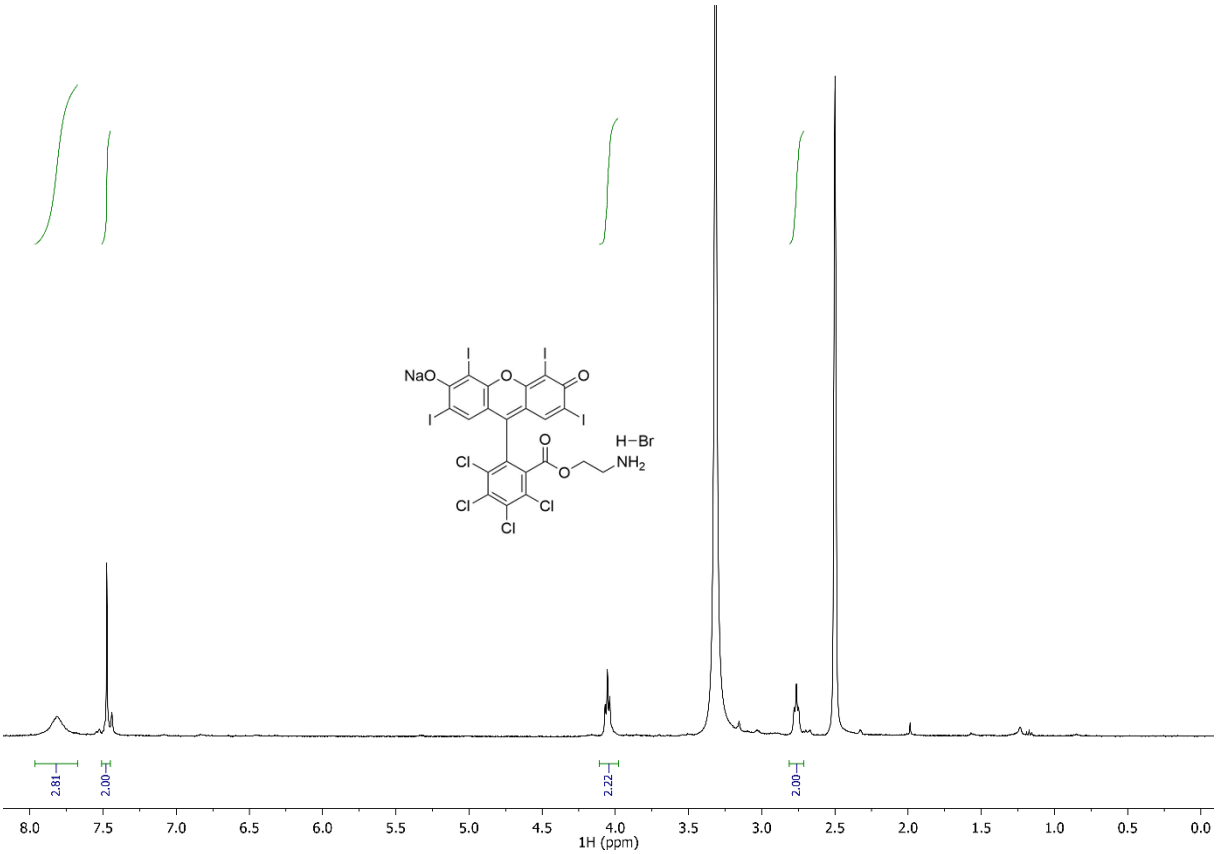

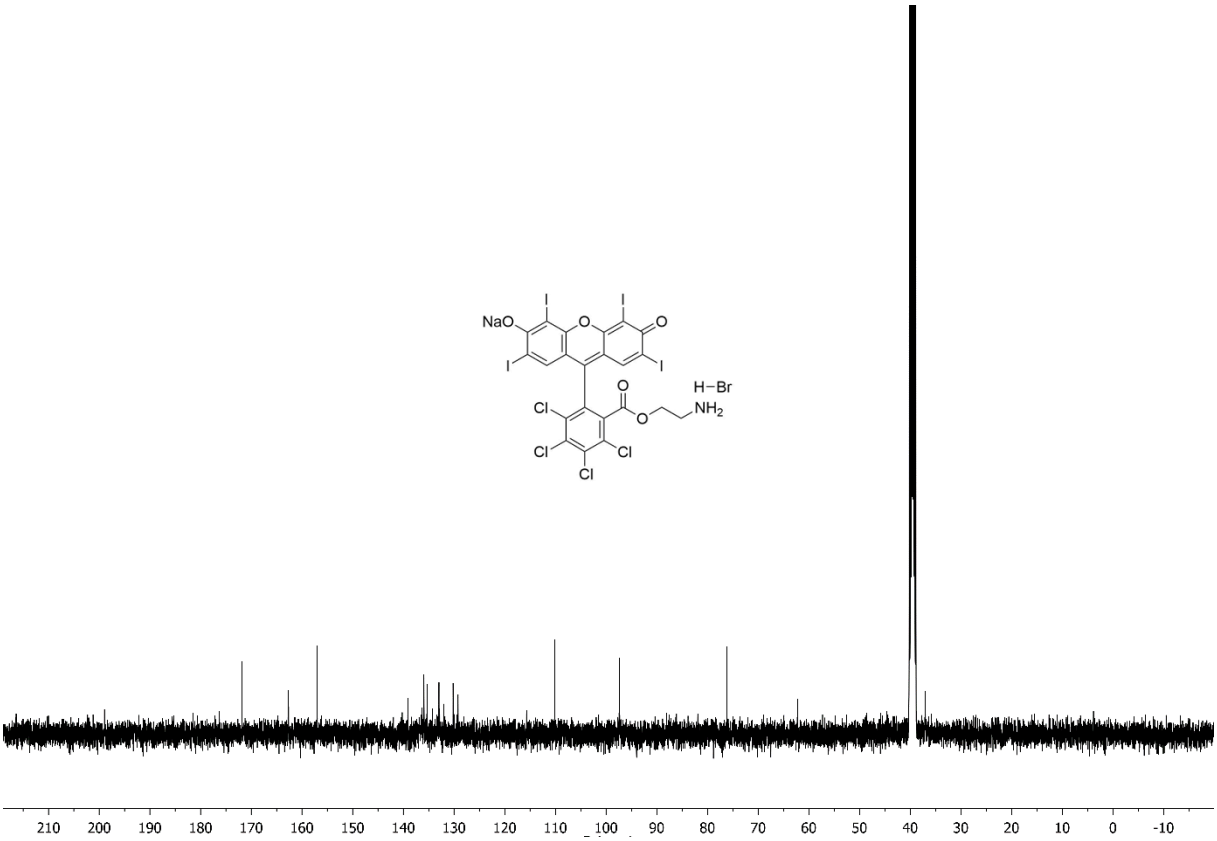

Figure S5. ^{1}H and ^{13}C NMR spectra of **3** in DMSO-d6.

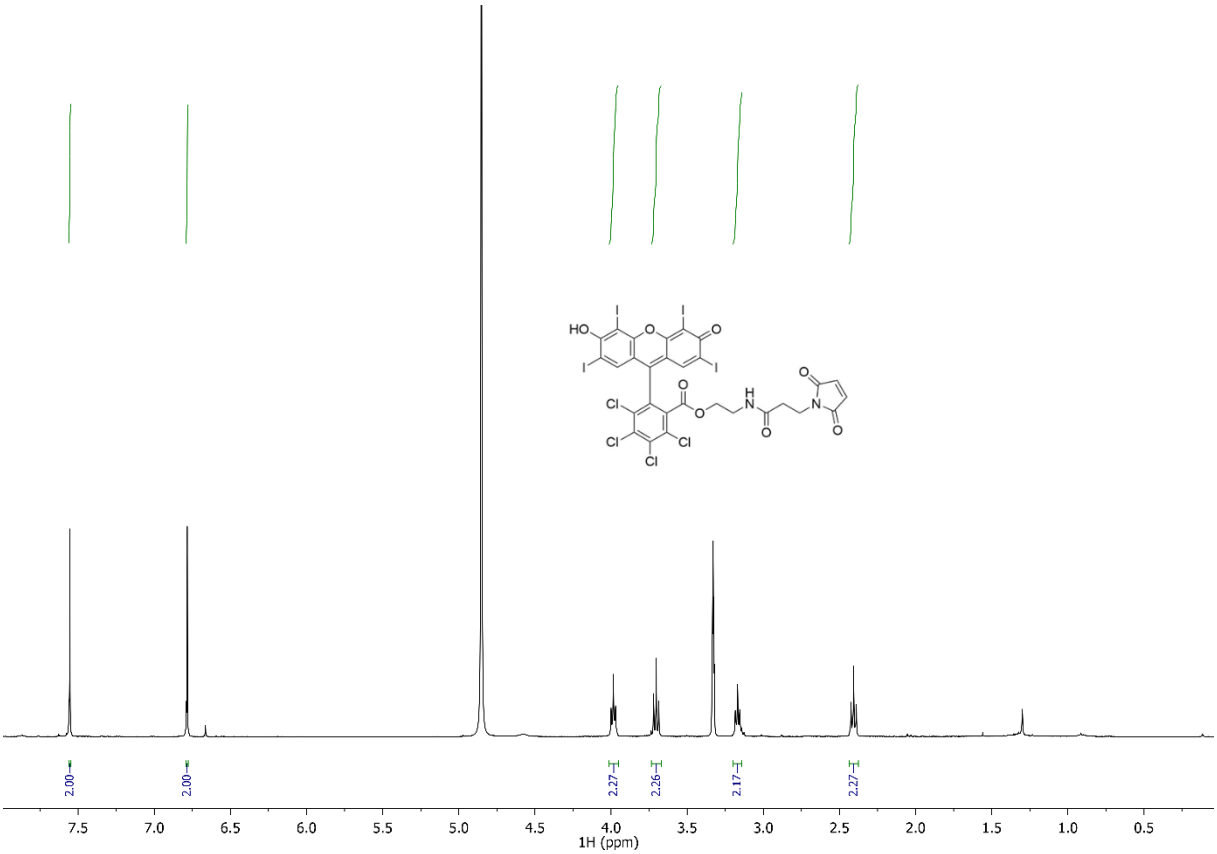

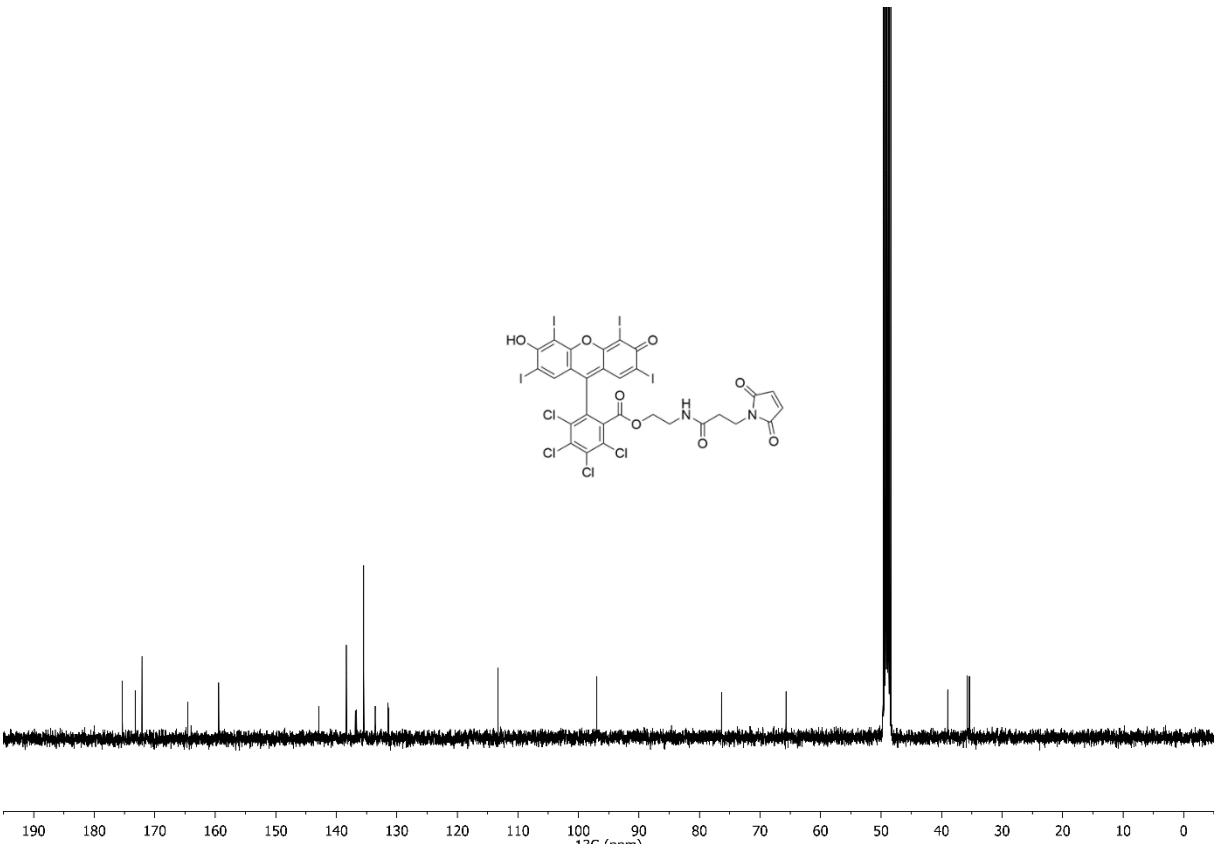

Figure S6. ^{1}H and ^{13}C NMR spectra of **4** in MeOD.

3.4 UV-Vis spectra

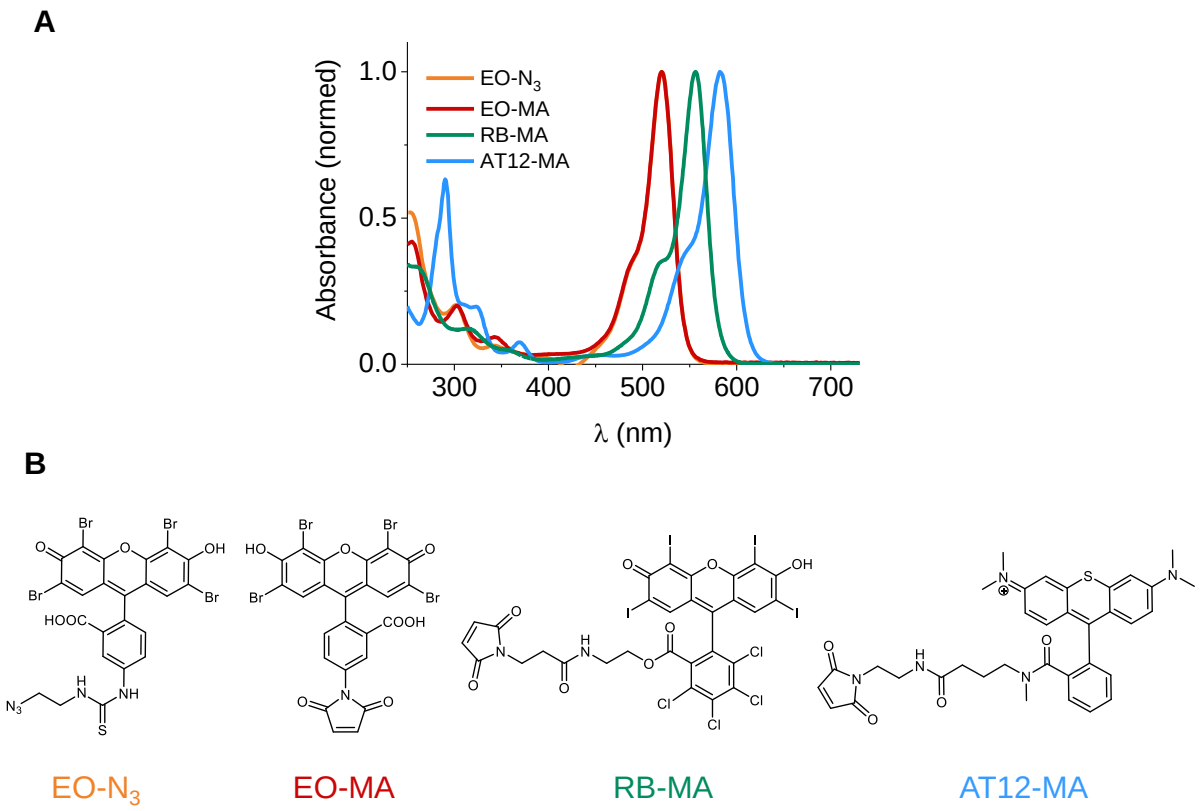

Figure S7. (A) Normalized UV-Vis spectra of the photoexcitable spin labels at r.t. in deionized water and (B) their chemical structures.

4. Molecular biology

4.1 Chemicals

Unless stated otherwise, all chemicals were obtained from Carl Roth or Sigma Aldrich. The non-canonical amino acid *para*-propargyloxy-*L*-phenylalanine (pPfF) was purchased from Iris Biotech GmbH. Atto Thio12 maleimide was obtained from AttoTec GmbH. Azido proxyl was synthesized according to published procedures.[18]

4.2 Site-directed mutagenesis and protein expression

The plasmids pBAD_TRX_His6_C33S_C36S_D14C_R74TAG and pBAD_TRX_His6_C33S_C36S were constructed by site-directed mutagenesis (QuikChange II Site-directed mutagenesis Kit, Agilent) of pBAD_TRX_His6 as described recently.[19]

Transformation of *E. coli*

Chemically competent BL21-Gold (DE3) *E. coli* cells were co-transformed with the plasmids pEVOL_pCNPhe, provided by the Schultz lab, and pBAD_TRX_His6_C33S_C36S_D14TAG_R74C. 100 µl of competent bacteria were thawed on ice, mixed with the appropriate amount of each plasmid and incubated on ice for 30 min. The cells were then heat-shocked at 42 °C for 45 s and incubated on ice for another 2 min before adding 1 mL pre-warmed (37 °C) Super Optimal Broth with carbolite repression (S.O.C.) medium. Afterwards, cells were incubated for 1 h at 37°C and 1400 rpm and then grown on LB-agar plates (Lennox) containing 50 µg/mL carbenicillin and 34 µg/mL chloramphenicol at 37 °C and 180 rpm overnight.

For glycerol stock creation, LB-medium containing 50 µg/mL carbenicillin and 34 µg/mL chloramphenicol was inoculated with a single colony from the agar plate and grown overnight at 37 °C and 180 rpm. 500 µl of the overnight culture were mixed with 50 % (v/v) glycerol in a 2 mL cryovial, shock-frozen in liquid nitrogen and stored at -80 °C.

Protein expression and purification

An overnight culture from the glycerol stock was grown in LB-medium supplemented with 50 µg/mL carbenicillin and 34 µg/mL chloramphenicol at 37 °C and 180 rpm. This starter culture was then diluted 1:100 with fresh LB-medium containing both antibiotics at the specified concentrations and allowed to grow at 37 °C and 180 rpm until an OD_{600} of 0.4 to 0.8 was reached. Protein expression was induced by adding 0.2 % (w/v) L-arabinose (20 % (w/v) stock solution, sterile-filtrated in deionized water) and solid *para*-propargyloxy-*L*-phenylalanine (pPfF) to the medium. After 12 h under these conditions, the cells were

harvested by centrifugation (4 °C, 3220 x g, 15 min) and the supernatant discarded. The cell pellet was resuspended in bacterial protein extraction reagent (B-PER, Thermo Fischer Scientific), 10 mM Tris-HCl (pH 7.4) supplemented with 1 mM phenylmethylsulfonylfluoride (PMSF) as protease-inhibitor. Cell lysis was done by sonification (Q700 QSONICA, cycles of 1 s pulse and 1 s pause for 60 s). For protein purification by Ni-NTA affinity chromatography, the resulting cell lysate was centrifuged (10 min, 15 000 rpm at 4 °C) and the supernatant transferred to a new tube containing Ni-NTA resin (His Pur). After 1 h of incubation at 4 °C, the beads were washed several times with washing buffer (50 mM NaH_2PO_4, 300 mM NaCl, pH 8, imidazole concentration increasing to 10 mM) before eluting TRX with the same buffer containing 500 mM imidazole. Protein concentrations were determined photometrically from the absorption at 280 nm on a Biophotometer D30 (Eppendorf). TRX was brought into PBS, pH 7.4 for maleimide and CuAAC labeling by dialysis.

4.3 Site-directed labeling

Maleimide coupling

The single-cysteine Trx mutant used in this work showed a strong propensity for forming intermolecular disulphide bonds, which is why the sulfhydryl-dependant maleimide labeling reaction was preceded by a reduction step with tris(2-carboxyethyl)phosphine hydrochloride (TCEP). For this purpose, 100 µM protein in PBS pH 7.5 was incubated with a twenty-fold excess of TCEP for 2-3 h at room temperature or at 4 °C overnight and subsequently passed over Zeba desalting columns (7K MWCO) equilibrated prior use with PBS pH 7.4 to remove TCEP as it is known to inhibit maleimide conjugation reactions. Then, 2 equivalents of the maleimide dyes (AttoThio12 maleimide, Rose Bengal maleimide) or 5 equivalents of Eosin maleimide (Sigma Aldrich) from 20 mM stock solutions in DMSO were added. For coupling with 3-maleimido-proxyl, a 10-fold excess (100 mM stock solution in DMSO) was added. All reactions were left to proceed for 1-2 h at 25 °C and 300 rpm in in an Eppendorf ThermoMixer C. Afterwards, surplus dye was removed by passing the labeling reaction over 1-3 Pierce™ Fluorescent Dye Removal Columns (Thermo Fischer Scientific) à 400 µl resin according to the manufacturer's instructions. Unreacted 3-maleimido-proxyl was removed with 8 washing steps with deionized water in Amicon Ultra Centrifugal Filters (0.5 mL centrifugal filters, 3.5 K MWCO, Merck; 15 min, 12 000 rpm, 4 °C).

CuAAC reaction

The CuAAC labeling reaction with the azido-proxyl label was performed as described previously.[2] Briefly, copper(II)-sulphate ($CuSO_4$) and the ligand 2-(4-((bis((1-(tert-butyl)-1H-1,2,3-triazol-4-yl)methyl)amino)methyl)-1H-1,2,3-triazol-1-yl) acetic acid (BTTAA) were mixed in deionized water in a 1:3 ratio. Ascorbic acid was added in a 1:1 ratio to reduce Cu(II) ions to the catalytically active Cu(I) species. The labeling reagents were then diluted with PBS buffer pH 7.4, and protein as well as azido-proxyl in DMSO

100 mM stock solution) were added, resulting in final concentrations of 1 mM copper(II)-sulfate, 3 mM BTTAA, 1 mM sodium ascorbate, 40 - 50 µM protein and 1 mM spin label. For the CuAAC reaction with Eosin-N_3, the concentration of the dye was reduced to 200 µM. The reaction was incubated at 25 °C and 800 rpm. Samples labelled with Eosin-N_3 were passed over two Dye Removal Columns à 400 µl resin prior to washing in Amicons as free dye was found to clog the membrane filter. In all cases, excess reagents were removed by washing steps in Amicon Ultra Centrifugal units. Protein samples were washed at least 4x with 400 µL PBS buffer containing 1 mM EDTA to chelate remaining copper ions, followed by a minimum of 4 further washing steps with 400 µl H_2O. The absence of free spin label was checked in wash solutions and for the negative controls (TRX mutants without cysteins) via cw-EPR measurements at an EMXnano spectrometer (Bruker Biospin), before lyophilizing the protein solution. Finally, the labelled protein was dissolved in D_2O.

4.4 Calculation of Dye Labeling Efficiency

UV-visible absorbance spectroscopy was used to determine the degree of labeling (DOL) of the purified dye-labelled protein according to the following equation[20]:

$$\mathrm{DOL}\ [\%] = \frac{\mathrm{A}_{\lambda,\mathrm{Dye}} * \varepsilon_{\mathrm{protein}}}{\left(\mathrm{A}_{280} - \mathrm{f} * \mathrm{A}_{\lambda,\mathrm{Dye}}\right) * \varepsilon_{\mathrm{Dye}}} * 100$$

Where $A_{\lambda,Dye}$ is the absorbance of the conjugate at a wavelength specific to the respective dye, ε_{Dye} is the extinction coefficient of the dye at this wavelength, A_{280} is the measured absorbance value at 280 nm and f is a correction factor for the dye's contribution to A_{280}. $\varepsilon_{protein}$ is the extinction coefficient of TRX at 280 nm (22 886 $M^{-1}cm^{-1}$)[19]. An overview of these parameters is provided in Table S1.

Table S1**.** Absorption parameters of dyes used for labeling.

	AT12-MA	**RB-MA**	**Eosin-N_3/MA**
λ_{Dye} (nm)	595	562	490
ε_{Dye} (M^{-1} cm^{-1})	73 900	38 000	20 280
f	0.7	0.4	0.66

The absorbance measurements were performed on an Eppendorf Biophotometer D30 using a µCuvette G1.0 with an optical path length of 1 mm.

5. EPR spectroscopy

5.1 X-band cw EPR spectroscopy

Room temperature cw EPR spectra were recorded at 20 °C on an EMX-Nano benchtop X-band spectrometer (Bruker). Typically, 10 µL of the purified protein sample was filled into a glass capillary (HIRSCHMANN ringcaps®; inner diameter 1.02 mm). Spectra were recorded with a modulation amplitude of 1 G, 3.162 mW microwave power, a sweep width of 200 G and a sweep time of 60 s. To improve the signal-to-noise ratio, the spectra were averaged over 16 - 20 scans. Quantitative spin concentrations were obtained using the built-in EMXnano reference-free spin counting module (Xenon software, Bruker), from which the labeling efficiency, defined as the ratio of spin to protein concentration, was calculated.

5.2 X-band time resolved EPR spectroscopy

Time resolved (tr) EPR measurements were performed at X-band (9.5 GHz) on a commercially available Bruker Elexsys E580 spectrometer (Bruker Biospin) with a microwave power of max. 3 mW. All measurements are performed in a critically coupled ER4118X-MS3 resonator (Bruker Biospin). Samples were held at cryogenic temperatures (10 K) with a CF935 helium gas flow system (Oxford Instruments) controlled by an ITC (Oxford Instruments). The spectrometer's built-in transient recorder and the laser were triggered by an external pulse generator with a repetition rate of 10 Hz. For each of the 1024 magnetic field positions, a 4096 ns long time trace was recorded (1024 time points at 4 ns time resolution). The spectra are shown in Figure S9.

5.3 Pulsed Q-band EPR measurements

Instrumentation

EPR spectrometer

All pulsed experiments were performed at Q-band (34 GHz) on a Bruker Elexsys E580 spectrometer equipped with a SpinJet-AWG unit (Bruker Biospin, Rheinstetten, Germany) and a 150 W pulsed TWT amplifier (Applied Systems Engineering, Fort Worth, USA). The temperature was maintained at 10 K with the EPR Flexline helium recirculation system (CE-FLEX-4K-0110, Bruker Biospin, ColdEdge Technologies), comprising a cold head (expander, SRDK-408D2) and a F-70H compressor (both SHI cryogenics, Tokyo,

Japan), controlled by an Oxford Instruments Mercury ITC. A commercial Q-band resonator (ER5106QT-2, Bruker Biospin) was used for all pulsed EPR measurements.

Laser system

Light excitation of the samples was achieved with the tunable diode pumped Nd:YAG laser system NT230-50-ATTN2-FC (EKSPLA, Vilnius, Lithuania) comprising a pump laser, second and third harmonics generators and an optical parametric oscillator (OPO). The system was operated with shot frequencies between 1 and 20 Hz and pulse energies of 3- 5 mJ. Triggering was performed by means of the spectrometer's pulse PatternJet (Q-band measurements) or an external pulse generator (trEPR measurements), and the light was coupled into the resonator using a quartz glass fibre (1 mm core, Pigtail WF 1000 / 1100 / 1600 T, CeramOptec GmbH, Bonn, Germany), the end of which was adjusted to a height of 1 cm above the sample surface.

Sample preparation

For EDFS and LaserIMD measurements, the purified protein samples in deionized water were lyophilized and reconstituted in D_2O. 60 % (v/v) of deuterated glycerol was added, resulting in a final spin concentration of 60 - 105 µM. A volume of 20 µl was transferred to a quartz tube with 3 mm outer diameter (fused quartz tubing, Technical Glass Products), degassed by several consecutive freeze-pump-thaw cycles and then shock-frozen in liquid nitrogen. For triplet relaxation measurements, 20 µl of a 200 µM solution of the free photoexcitable spin labels in D_2O/glycerol-d8 40/60 (v/v) was prepared in the same manner as described for the protein samples, as were the samples for trEPR measurements. For the latter, a solution of 1 mM of the free photoexcitable spin labels was used.

EPR experiments

All pulsed EPR experiments were performed at Q band (34 GHz) with a microwave attenuation of 0 dB, corresponding to a microwave power of 20 mW. Echo signals were detected in integrator mode with a video bandwidth of 200 MHz. The integrator gate width was chosen as the full width at half maximum (FWHM) of the echo. The shot repetition rate was chosen according to the triplet relaxation time.

EDFS

Echo-detected field swept spectra were recorded at 10 K employing a standard Hahn echo sequence (Laser-DAF-$\pi/2 - \tau - \pi - \tau$ – echo), with an interpulse delay of τ = 800 ns and a DAF of 500 ns. Pulse lengths were optimized with a nutation experiment, usually 6 - 8 ns for a π-pulse. The spectra were recorded with 1 - 10 shots per point and averaged over 1 - 5 scans to improve the signal to noise ratio.

Triplet relaxation

The relaxation of the triplet states of the free chromophores in solution was measured by plotting the integral of the Hahn echo for increasing values of the delay after flash (DAF) at field positions corresponding to the emissive Y canonical orientation of the zero-field splitting at 10 K. Based on the parameters obtained from trEPR experiments (Figure S9), Eosin-MA was believed to show relaxation behaviour similar to that of Eosin-N_3 and was not measured separately. The decay curves were recorded at laser shot frequencies of 1 Hz and with 1 shot per point. The DAF was incremented in steps of 500 µs (AT12-MA, 60 scans), 10 µs (RB-MA, 5 scans) or 1 µs (Eosin-N_3, 4 scans). However, using the DAF value at which the triplet signal had decayed completely as the shot repetition time (SRT) appeared to be insufficient for complete relaxation of the triplet state in the case of RB-MA and AT12, as the integral of the Hahn echo increased for higher SRTs. Consequently, the repetition rate for all further experiments was adjusted by monitoring the integral of the Hahn echo for different SRTs. This resulted in shot frequencies of 1 Hz (AT12-MA), 16 Hz (Eosin-N3 and Eosin-MA) and 20 Hz (RB-MA). The phase memory times were not considered, as they are not relevant for LaserIMD.

Resonator profile

Resonator profiles were measured by determining the m.w. field strength $\upsilon 1$ as nutation frequency at different m.w. frequencies, as described in literature[21]. Nutation experiments were performed over a frequency window of 300 MHz in 10 MHz steps. The magnetic field was co-stepped to retain correct observer pulse flip angles. Nutation frequencies were determined by Fourier transformation of the resulting nutation traces.

LaserIMD

LaserIMD experiments were performed in an critically coupled resonator with the pulse sequence reported by Hintze *et al.*[8] ($\pi/2$ - τ - π - t - laser pulse - (τ – t) – echo). Data was recorded at 10 K with τ = 5000 µs (AT12-MA, RB-MA, EO-N_3) or τ = 4000 µs (EO-MA) and 1 shot per point. A 2-step phase cycle was applied on the first observer pulse to cancel receiver offsets. Both the forward and the reverse LaserIMD traces were recorded, although only the forward trace was analysed for the data shown. All LaserIMD measurements were performed as 2D experiments, and each scan was phase-corrected individually during post-processing. 24 scans were summed for each LaserIMD measurement. Details on wavelength, SRT, spin and dye concentrations are provided in Table S4.

4-pulse-DEER

4-pulse DEER measurements were performed at 50 K in an overcoupled resonator with a Q value typically around 200 (resonator profile in Figure S11). 4-pulse DEER data were recorded with the pulse sequence $(\pi/2)_{obs} – \tau_1 – \pi_{obs}$ - t – t_{pump} - ($\tau_1 + \tau_2 – t$) – $\pi_{obs} – \tau_2$ – echo[22], with interpulse delays of τ_1 = 400 ns, τ_2 = 8 µs

while the pump pulse positions was incremented in t = 8 ns steps. Nuclear modulation artifacts were suppressed by averaging 8 traces with varied interpulse delay τ_1 by $\Delta\tau_1$ = 16 ns. A 2-step phase cycle [+(+x)-(-x)] on the π/2-observer and 4 steps [+(+x)-(+y)+(-x)-(-y)] on the π observer pulse were used to remove other echoes capable of interfering with the detected signal as suggested by Tait and Stoll.[23] Gaussian observer pulses with lengths $t_{\pi/2}$ = 30-32 ns and t_π = 60-64 ns were used. The pump pulse was a 90 MHz broad HS[1] pulse with t_π = 100 ns and β/t = 8 that was set to match the nitroxide and resonator maximum at an frequency offset of +90 MHz to the observer pulses. It was calculated with MATLAB (version 2018b) using the function "pulse" of the easyspin software package.[24] 70 scans were recorded with one shot per point and a shot repetition time of 4080 μs.

Distance analysis

The forward trace of LaserIMD data was evaluated with DeerAnalysis 2019.[25] The zero time was determined manually, and the starting times for background fits (3-dimensional homogenous background) were determined automatically by the program. Extraction of the distance distribution from the resulting form factor, obtained by background division, was achieved with model-free Tikhonov regularization, using the generalized cross-validation (GVC) criterion to determine the optimum regularization parameter α. The resulting distance distributions were validated using the validation tool included in the DeerAnalysis2019 software by varying the background start (20 different values in a range of 1000 ns), noise level (2 different values) and background dimension (6 values between 1.5 and 3.0) during the regularization procedure with a prune level of 1.15. Uncertainties are depicted as shaded areas in the distance distributions.

TrEPR spectral analysis[26]

2D trEPR data were baseline corrected. 1D spectra were obtained by a summation over a range from 100 ns to 400 ns after the laser excitation. The Simulations of the spectra were performed using a home-written MATLAB (version 2019b) program based on the 'pepper' function of the MATLAB toolbox EasySpin (easyspin-5.2.28)[24]. For the simulations, an isotropic *g* value of 2 and an additional linewidth of 2 mT[26] were set and the ZFS values including a D_{strain} and the relative triplet sublevel populations were adjusted.

6. EPR data

6.1 CW spectra

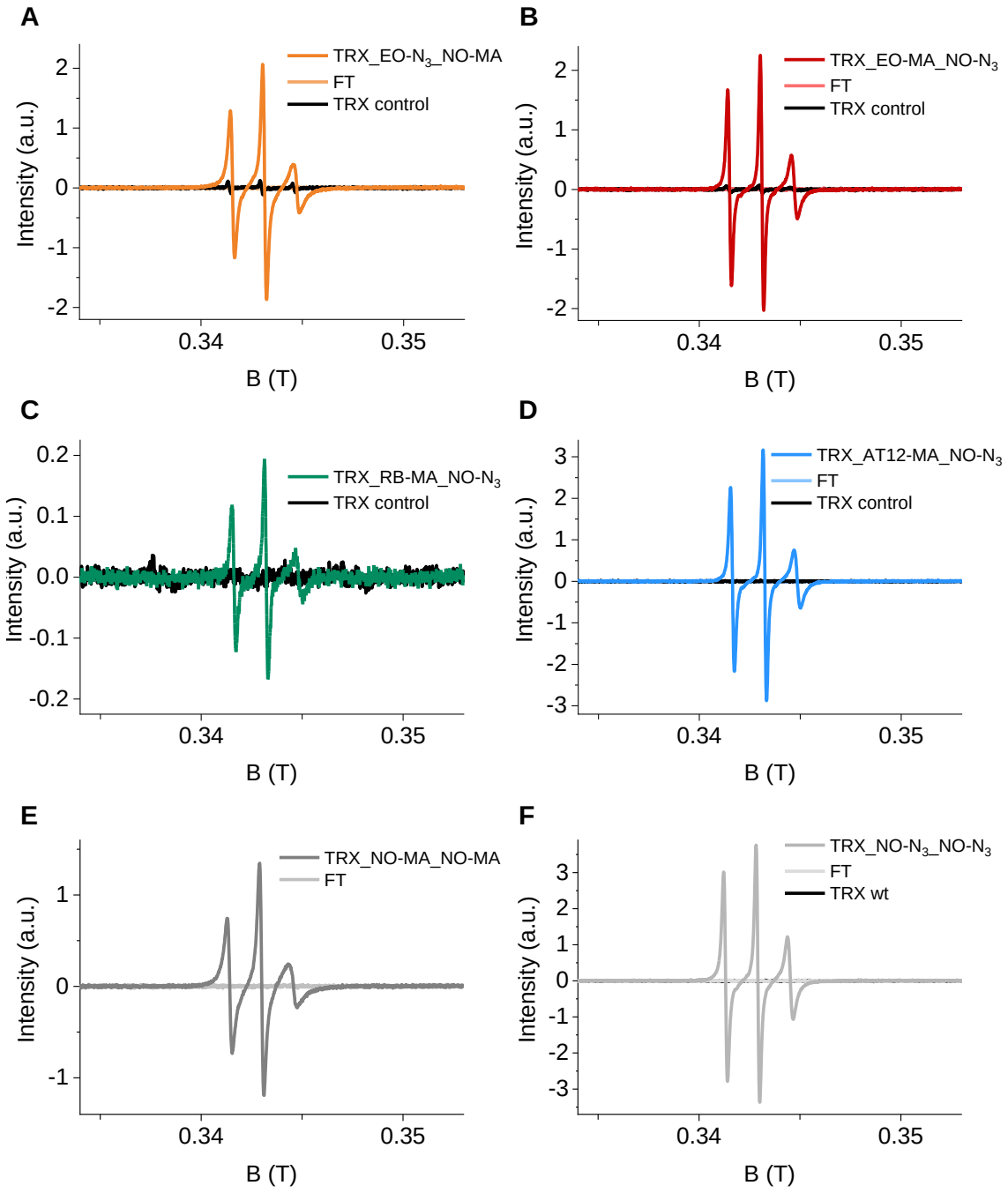

Figure S8. cw-EPR spectra of TRX doubly labeled with different spin labels at positions 14 and 74, confirming the attachment of the nitroxide spin label. (A) Trx_EO-N3_NO-MA, (B): Trx_EO-MA_NO-N3, (C) Trx_RB-MA_NO-N3, (D) Trx_AT12-MA_NO-N3, (E) Trx_NO-MA_NO-MA, (D) Trx_NO-N3_ NO-N3. The spectra of the flow-through (FT) were recorded to prove efficient removal of free spin label. TRX_C33S_C36S (TRX control) and TRX wild-type (wt) were labelled under the same conditions and serve as negative controls; the respective cw-spectra are shown in black.

6.2 trEPR spectra

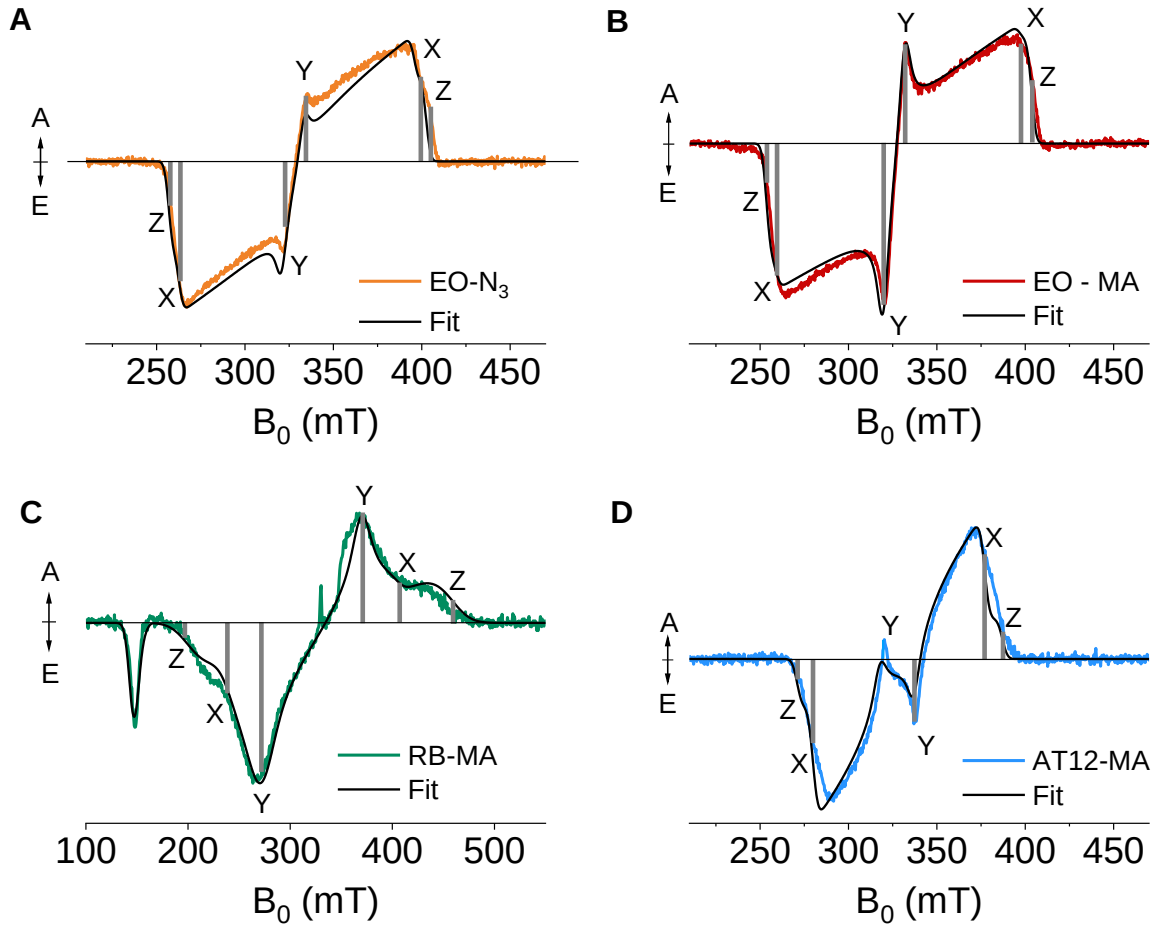

Figure S9. Time-resolved EPR spectra of the chromophores used in this work. The field positions of the canonical orientations of the zero-field splitting are represented as grey bars. Spectral simulations, shown as black lines, were used to determine the zero-field splitting parameters |D| and |E| and the zero-field populations p_x, p_y and p_z. Assuming an oblate spin-density distribution, which is common in planar aromatic systems, D > 0 and E < 0. Data was collected at 10 K with a microwave frequency of 9.5 GHz. (A): Eosin-N_3 (|D| = 2054 MHz, |E| = 585 MHz, D_{strain} = 362.2 MHz; p_x = 0.44, p_y = 0.48, p_z = 0.08). (B): Eosin-MA (|D| = 2093 MHz, |E| = 593.7 MHz, D_{strain} = 303.4 MHz; p_x = 0.38, p_y = 0.62, p_z = 0). (C): RB-MA (|D| = 3671 MHz, |E| = 319 MHz, D_{strain} = 942.3 MHz; p_x = 0.1, p_y = 0.52, p_z = 0.38). (D): AT12-MA (|D| = 1638.3 MHz, |E| = 375.3 MHz, D_{strain} = 598.2 MHz; p_x = 0.86, p_y = 0.03, p_z = 0.11). For all simulations an additional linewidth of 2 mT and a g value of 2 was used.

6.3 EDFS spectra

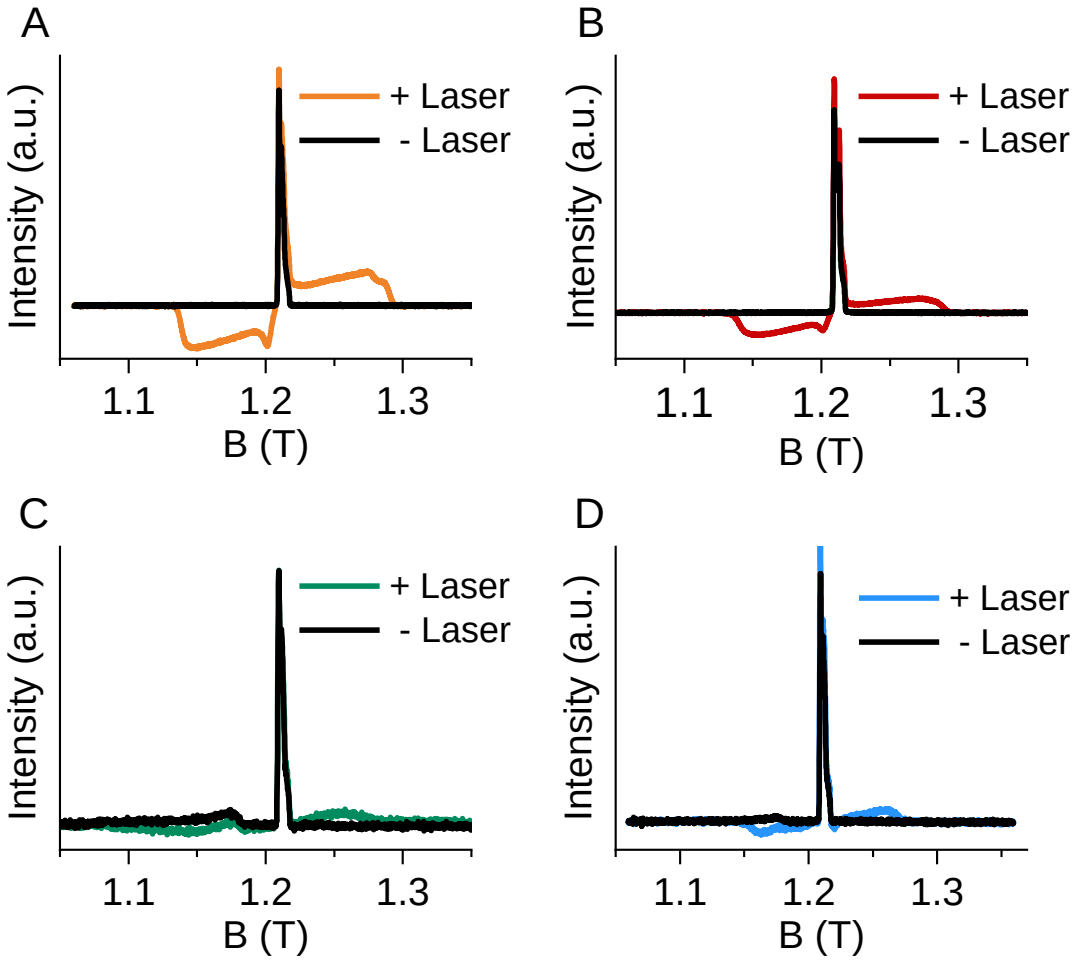

Figure S10. EDFS spectra of TRX in Q-band, labeled with a photoexcitable spin label and a nitroxide at positions 14 (CuAAC) and 74 (Cys-maleimide coupling), without (black) and with (color) light excitation at wavelength λ. (A) EO-N_3/NO-MA, λ = 510 nm, (B) EO-MA/NO-N_3, λ = 510 nm, (C) RB-MA/NO-N_3, λ = 550 nm, D) AT12-MA/NO-N_3, λ = 582 nm. The broad signal from 0.9 to 1.19 T with and without light excitation in (C) and (D) arises from residual Cu(II) from the CuAAC reaction.

6.4 Resonator profile

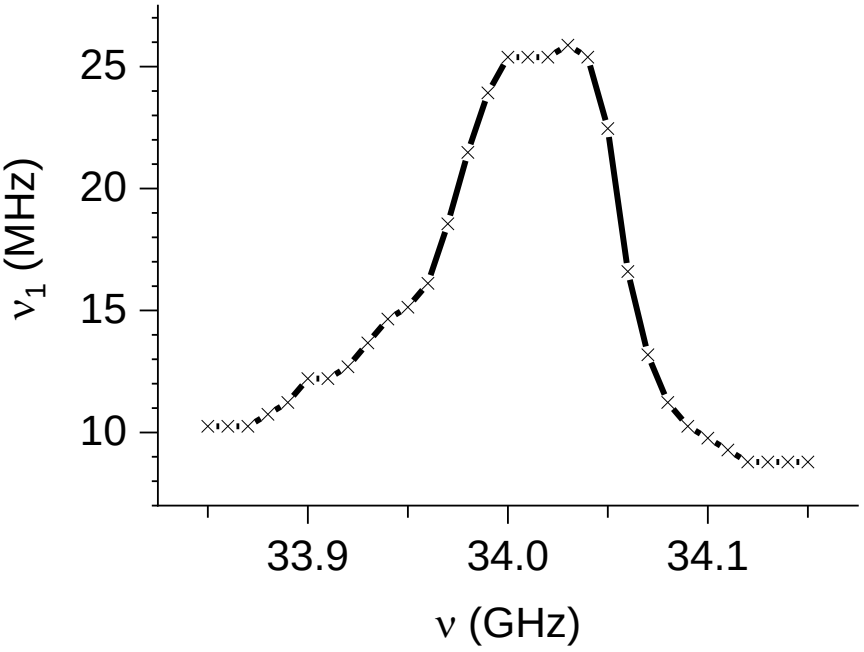

Figure S11. Experimentally determined resonator profile of the overcoupled QTII resonator (Bruker).

6.5 Triplet relaxation

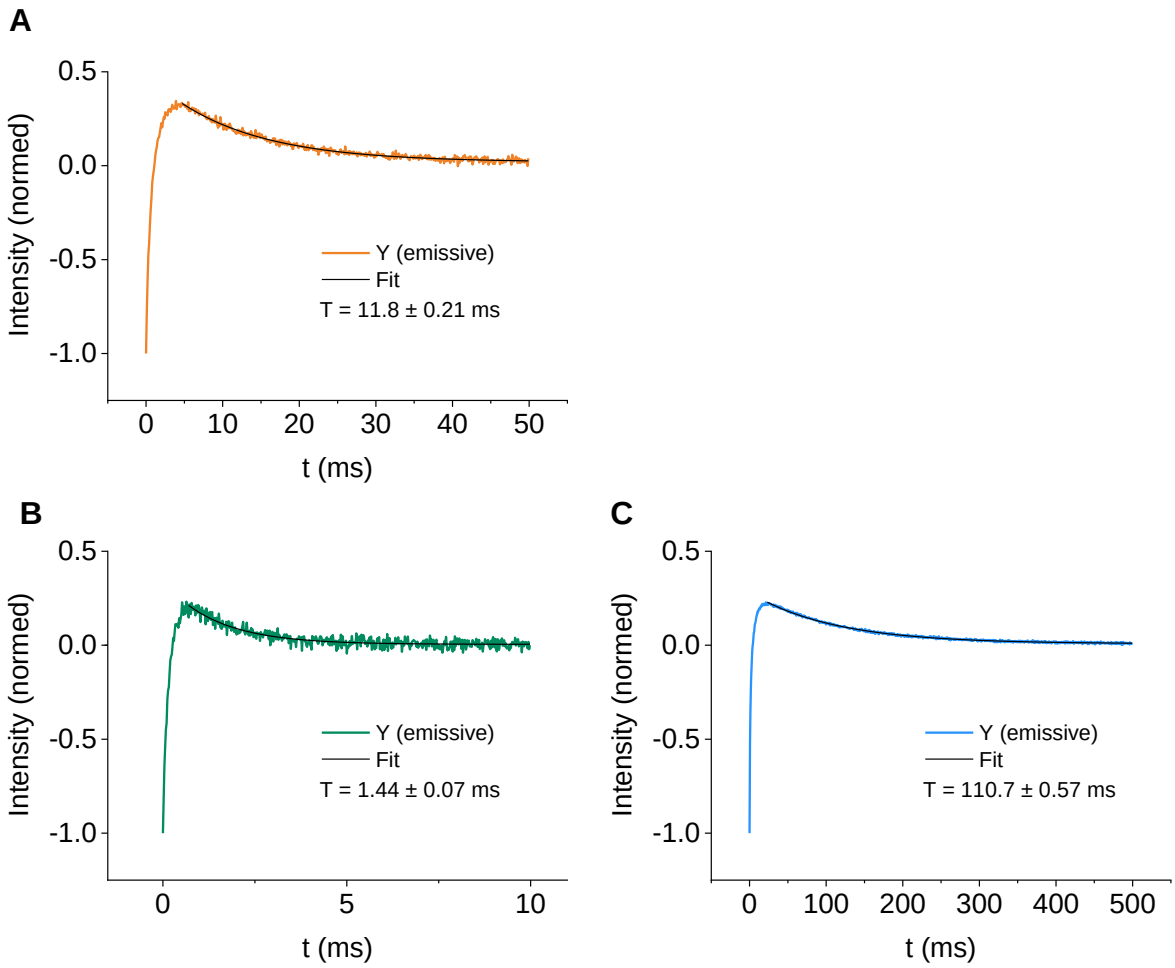

Figure S12. Integrated Hahn-echo intensities as a function of the delay after flash of the dye labels. The spectra were collected at field positions corresponding to the emissive transition of the Y canonical orientation of the zero-field splitting. (A) Eosin-N_3 (1.2 T), (B) RB-MA (1.15 T), (C) AT12-MA (1.22 T). The later part of the decay curve, representing the relaxation of the triplet state, was fitted with a mono-exponential decay function.

6.6 LaserIMD

Eosin-N_3

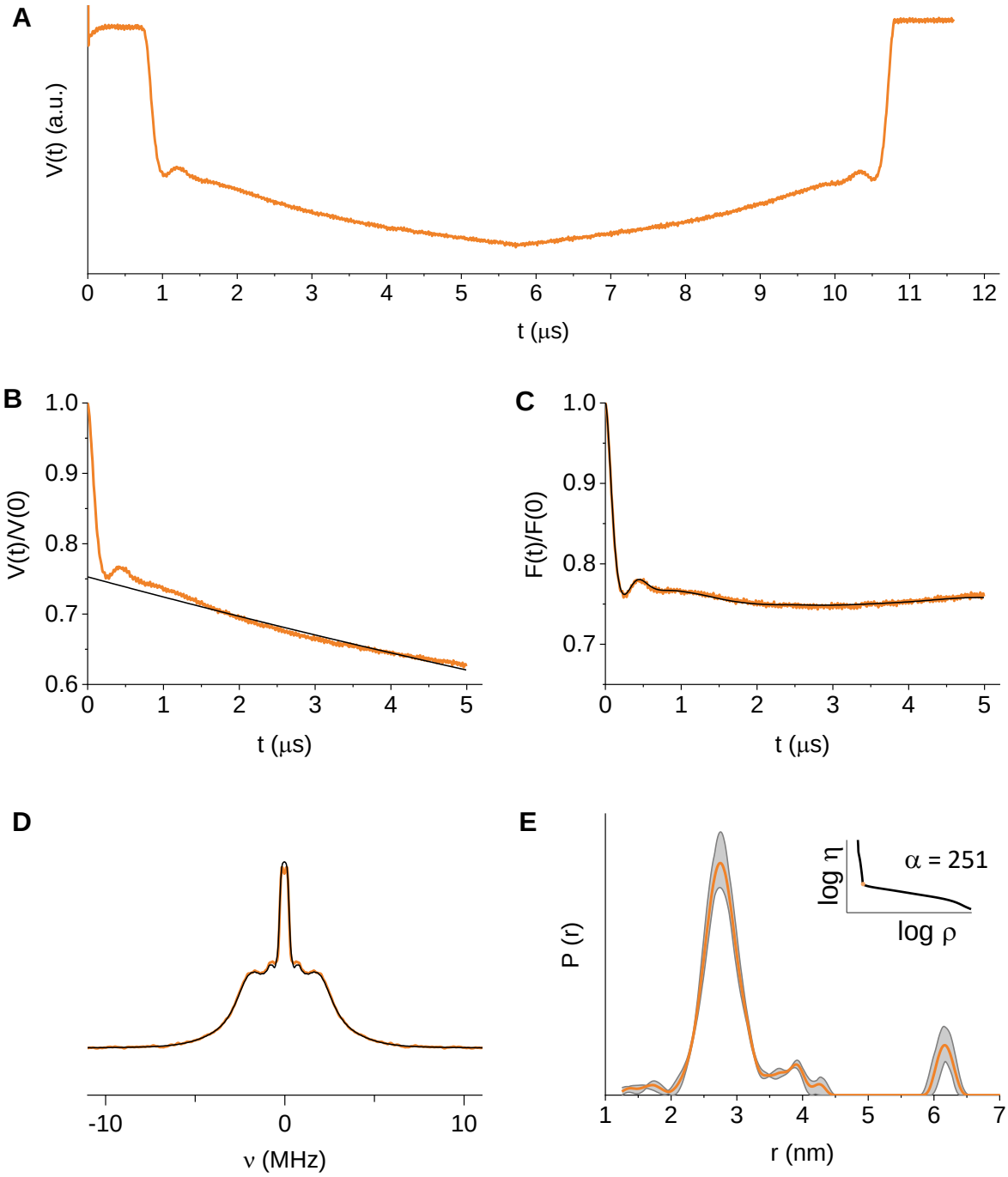

Figure S13. LaserIMD d**istance** measurement on TRX labelled with Eosin-N_3 at position 14 (CuCAAC) and NO-MA at position 74 (Cys-maleimide coupling). (A) Full LaserIMD trace (real part) with forward and reverse part. (B) Forward part of the normalized LaserIMD trace with 3-dimensional homogenous background fit. (C) Background corrected form factor, modulation depth of 25 %, with fit by Tikhonov regularization. (D) Dipolar spectrum obtained by Fourier transformation. (E) Validated distance distribution obtained by Tikhonov regularization. The L-curve is shown as inset with indicated α-parameter, automatically determined by the GCV criterion. For all traces, experimental data are shown in orange and corresponding fits in black.

Eosin-MA

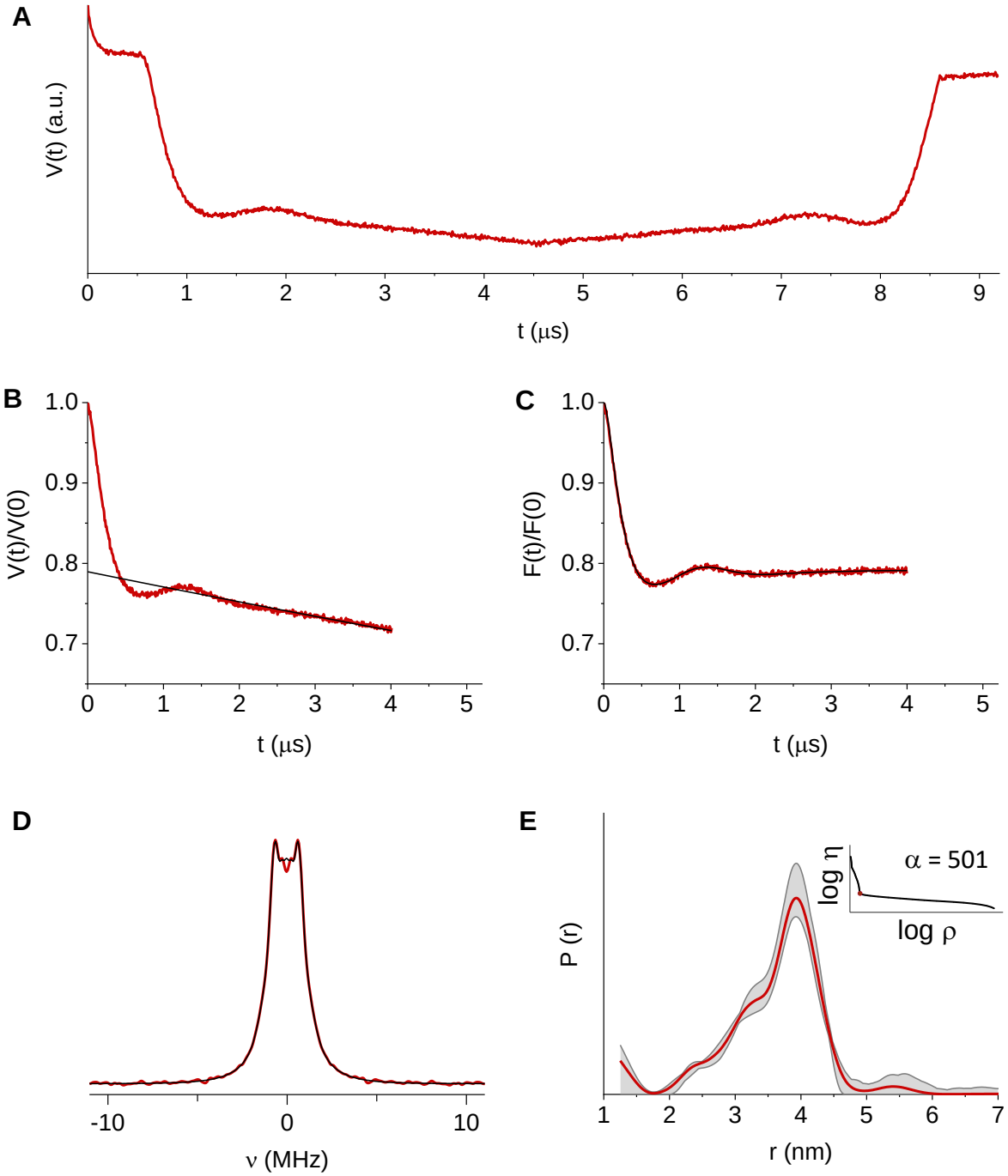

Figure S14. LaserIMD distance measurement on TRX labelled with Eosin-MA at position 74 (Cys-maleimide coupling) and NO-N_3 at position 14 (CuCAAC). (A) Full LaserIMD trace (real part) with forward and reverse part. (B) Forward part of the normalized LaserIMD trace with 3-dimensional homogenous background fit. (C) Background corrected form factor, modulation depth of 21 %, with fit by Tikhonov regularization. (D) Dipolar spectrum obtained by Fourier transformation. (E) Validated distance distribution obtained by Tikhonov regularization. The L-curve is shown as inset with indicated α-parameter, automatically determined by the GCV criterion. For all traces, experimental data are shown in red and corresponding fits in black.

RB-MA

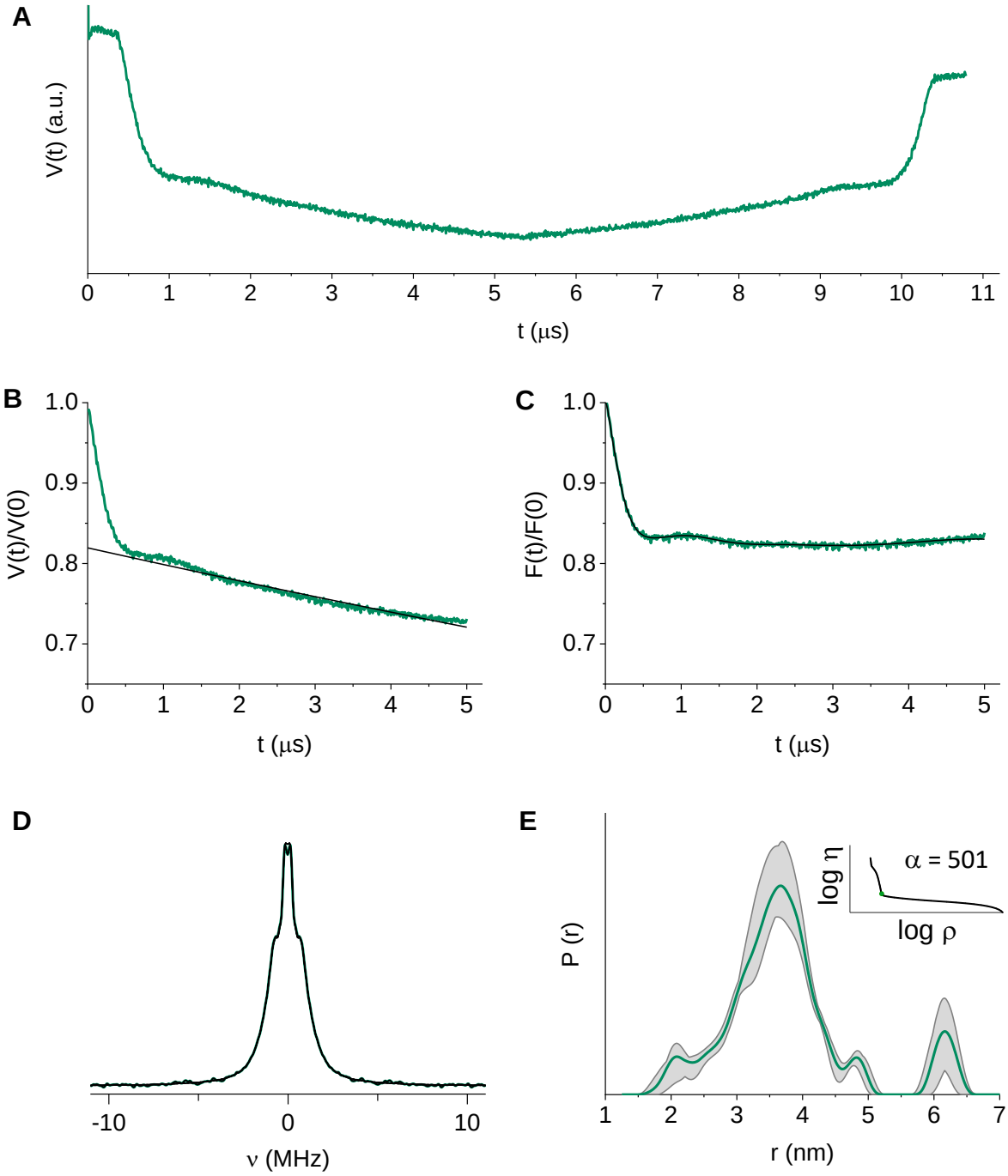

Figure S15. LaserIMD distance measurement on TRX labelled with RB-MA at position 74 (Cys-maleimide coupling) and NO-N_3 at position 14 (CuCAAC). (A) Full LaserIMD trace (real part) with forward and reverse part. (B) Forward part of the normalized LaserIMD trace with 3-dimensional homogenous background fit. (C) Background corrected form factor, modulation depth of 18 %, with fit by Tikhonov regularization. (D) Dipolar spectrum obtained by Fourier transformation. (E) Validated distance distribution obtained by Tikhonov regularization. The L-curve is shown as inset with indicated α-parameter, automatically determined by the GCV criterion. For all traces, experimental data are shown in red and corresponding fits in black.

AT12-MA

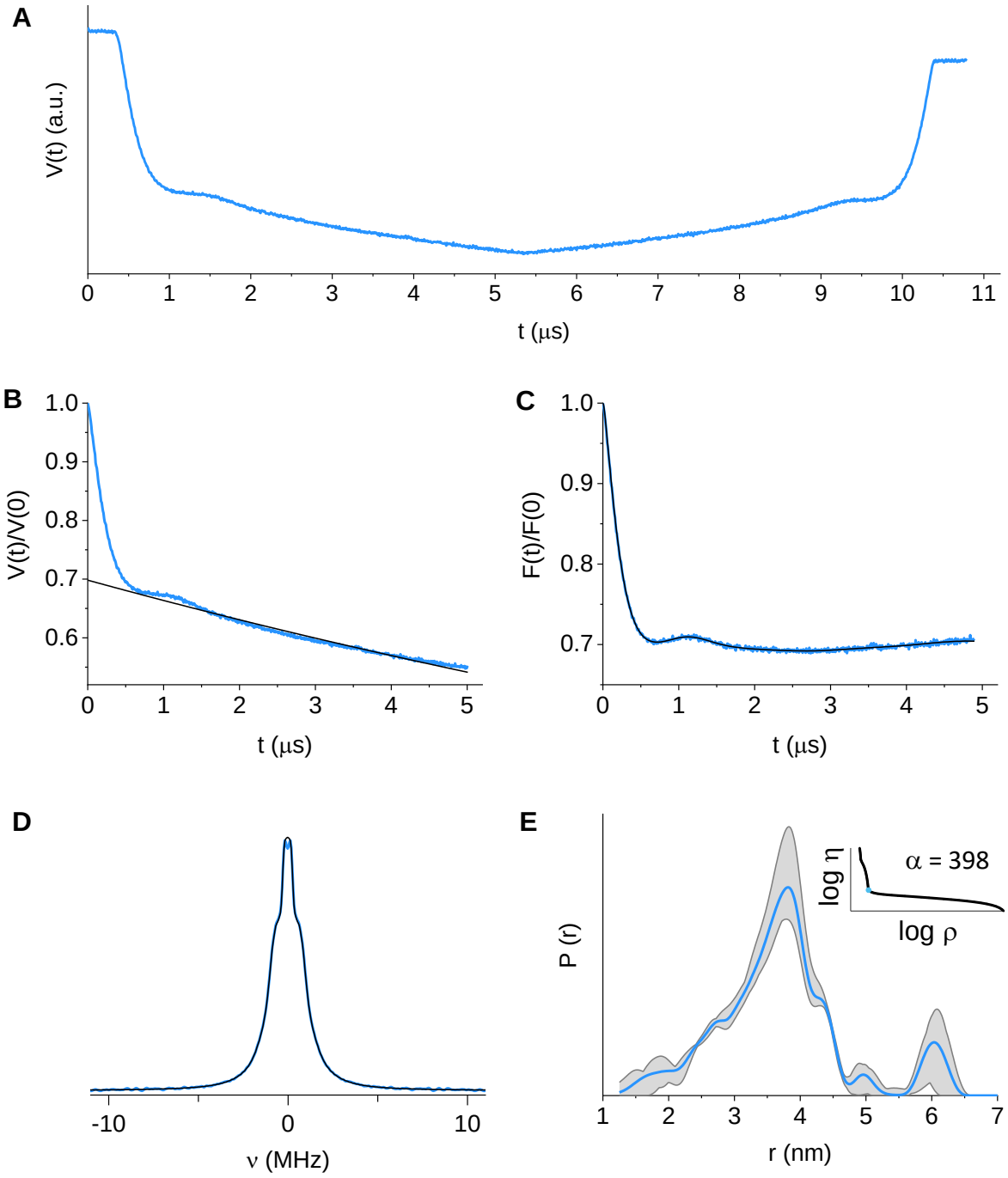

Figure S16. LaserIMD distance measurement on TRX labelled with AT12-MA at position 74 (Cys-maleimide coupling) and NO-N_3 at position 14 (CuCAAC). (A) Full LaserIMD trace (real part) with forward and reverse part. (B) Forward part of the normalized LaserIMD trace with 3-dimensional homogenous background fit. (C) Background corrected form factor, modulation depth of 31 %, with fit by Tikhonov regularization. (D) Dipolar spectrum obtained by Fourier transformation. (E) Validated distance distribution obtained by Tikhonov regularization. The L-curve is shown as inset with indicated α-parameter, automatically determined by the GCV criterion. For all traces, experimental data are shown in red and corresponding fits in black.

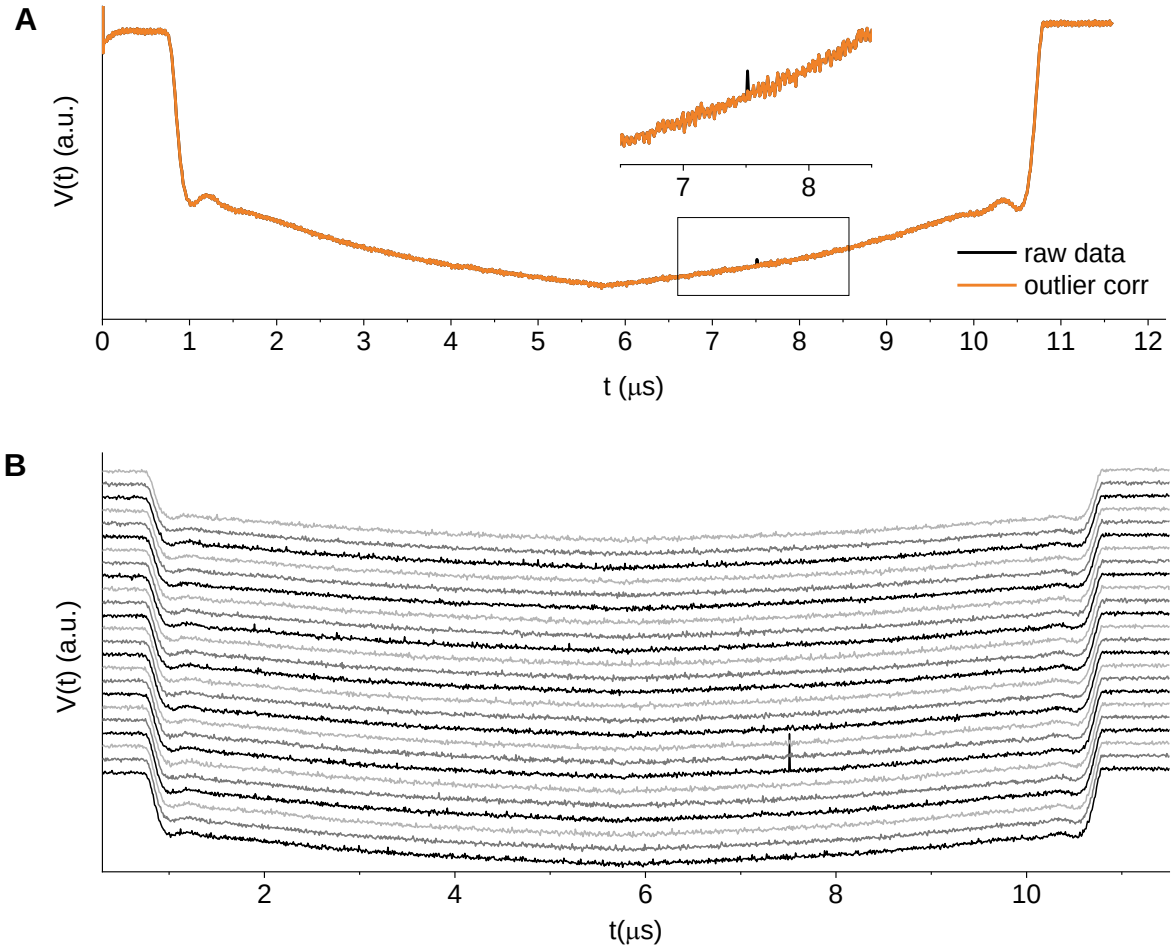

Figure S17. Outlier analysis for the LaserIMD raw data of EO-N_3 and NO-MA labelled TRX. (A) The mean of 24 LaserIMD scans with (orange) and without (black) correction of the one data point in the seventh scan that lies factor 10 higher than other values. (B) All 24 raw data scans from the dipolar evolution trace are shown with an offset for clarity. From these traces, the "spike" in the seventh scan at 7.5 µs was identified as outlier. This single point was replaced by the mean value of the corresponding value in the 6^{th} and 8^{th} scan for further data analysis.

6.7 Four-pulse DEER

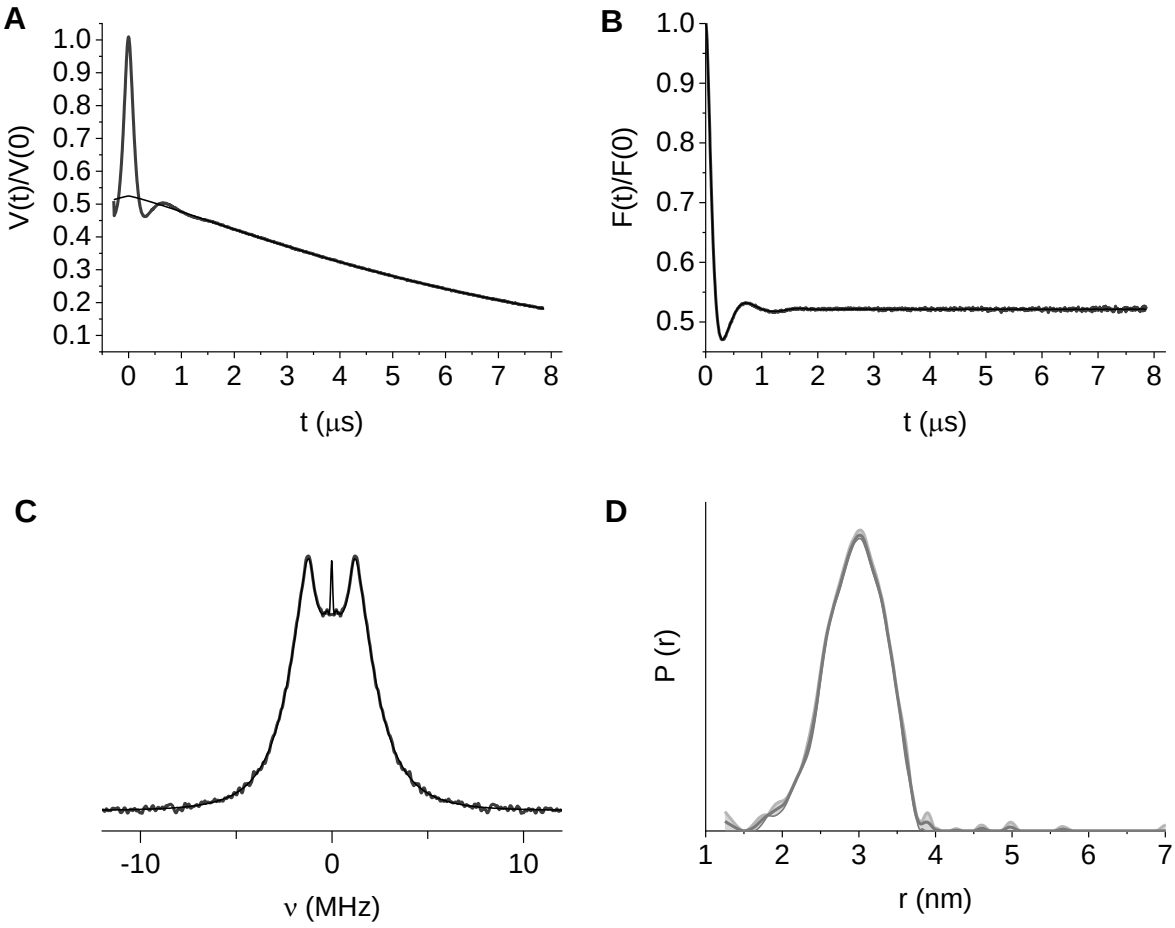

Figure S18. Four-pulse DEER data from TRX doubly labelled with NO-MA at position 14 and 74 via Cys-maleimido coupling. (A) DEER trace (real part) trace with a 3.50-dimensional homogenous background, which was necessary to fit the experimental data. (B) Background corrected form factor with a modulation depth of 48 %. (C) Dipolar spectrum obtained by Fourier transformation. (D) Validated distance distribution obtained by Tikhonov regularization. The α-parameter of 200 was automatically determined by the GCV criterion. Fits are shown in black for all traces. A 100 ns long, 90 MHz broad HS{1,1} pump pulse (β = 8) was set to the nitroxide and resonator maximum with an offset of 90 MHz to the Gauss observer pulses with a π-pulse length of 64 ns. 70 scans were acquired with one shot per point.

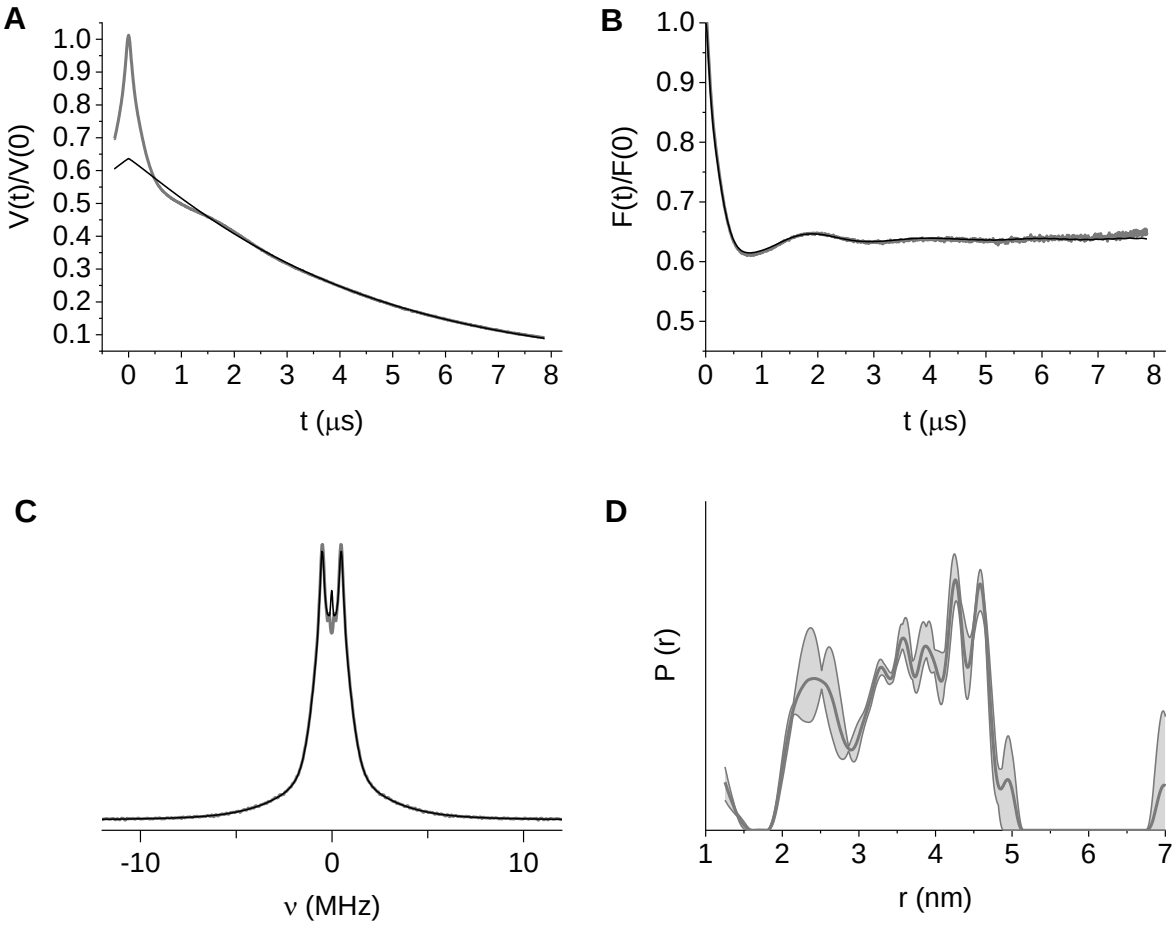

Figure S19. Four-pulse DEER data from TRX doubly labelled with NO-N_3. at position 14 and 74 via CuCAAC. (A) DEER trace (real part) trace. A 3.25-dimensional homogenous background was necessary to fit the experimental data. (B) Background corrected form factor with a modulation depth of 36 %. (C) Dipolar spectrum obtained by Fourier transformation. (D) Validated distance distribution obtained by Tikhonov regularization. The α-parameter of 398 was automatically determined by the GCV criterion. Fits are shown in black for all traces. A 100 ns long, 90 MHz broad HS{1,1} pump pulse (β = 8) was set to the nitroxide and resonator maximum with an offset of 90 MHz to the Gauss observer pulses with a π-pulse length of 60 ns. 70 scans were acquired with one shot per point.

Table S2. Summary of obtained distance distributions. The width of the distance is given as standard deviation of validated distance distributions.

Sample	Modulation depth (%)	Mean of distance distribution <r> (nm)	Global max. of distance distribution r_{max} (nm)	Width of distance distribution <s> (nm)
Eosin-N_3	24.5	3.2	2.8	1.1
Eosin-MA	21.0	3.7	3.9	0.7
RB-MA	18.1	3.8	3.7	1.0
AT12-MA	30.5	3.7	3.8	1.0
NO-MA	47.5	2.9	3.0	0.4
NO-N_3	36.3	3.5	4.6	0.9

Contributions at around 6 – 6.5 nm in the P(r) vs r(nm) plots shown in Fig S13, S15 and S16 are not considered to be reliable, as the dipolar evolution time t_{max} of 5 µs only allows distances up to approximately 6.8 nm (according to $r_{max} = 5 \cdot \sqrt[3]{\frac{t_{max}}{2\ \mu s}}\ nm$ [27]) to be determined accurately. This is supported by the lack of distances exceeding 5 nm in the DEER traces with longer dipolar evolution times (8 µs, r_{max} = 8 nm).

Effect of photobleaching

24 scans with one shot-per-point were accumulated for all triplet labels, which allowed us to make a crude estimation of the compounds' photostability under conditions typical for pulsed EPR experiments. Photobleaching is a phenomenon whereby reactions between the fluorophore in its excited long-lived triplet state and surrounding molecules are believed to lead to structural alterations that cause the dye to lose its ability to fluoresce.[28] In LaserIMD, such fading processes reduce the number of pump spins for optical switching and consequently result in a loss of modulation depth. Table S3 and Figure S20 show the decrease in modulation depth and triplet signal intensity, respectively, which occurred during the LaserIMD experiments and was attributed to photobleaching.

Table S3. Decrease in modulation depth during the LaserIMD experiments shown in 6.6, presumably caused by photobleaching of the chromophores. The values only provide a trend for the photostability of the dyes, as sample concentration, excitation wavelength and laser energy differ between measurements and less points were accumulated for the Eosin-MA sample.

Sample	Modulation depth (%) 1st scan	Modulation depth (%) 24th scan	Relative decrease modulation depth (%)
Eosin-N_3	28.6	21.9	23
Eosin-MA	22.1	19.7	11
RB-MA	22.8	14.7	36
AT12-MA	30.2	29.2	3

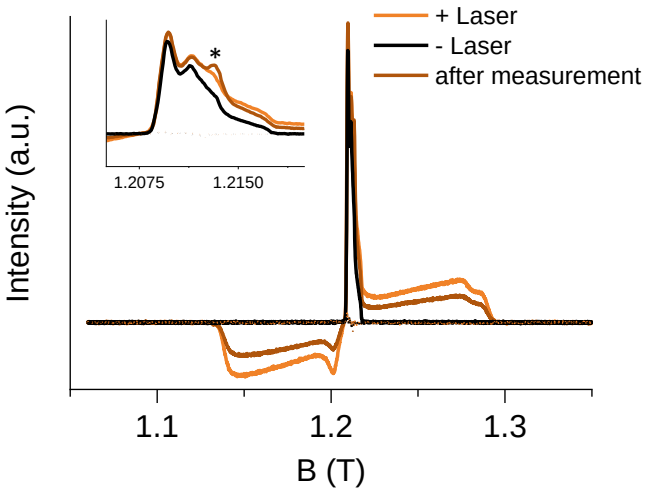

Figure S20. EDFS spectrum of TRX labeled with EO-N_3 and EO-MA without light excitation (black), with light excitation before the LaserIMD experiment (orange) and after completion of 24 scans (brown). In the inset, the formation of an illumination-induced persistent radical is marked with an asterisk.

Influence of radicals formed upon sample illumination

The presence of the persistent radical shown in Figure S20 may impact the dipolar pattern and result in additional distances in the distance distribution. Consequently, the formation of this species was studied in more detail:

- The radical is linked to the photoexcitable labels, as it does not appear when the LaserIMD measurements described for doubly labelled TRX are performed on a 100 µM solution of 3-maleimido-PROXYL in 60/40 glycerol/water at 10 K (Figure S21 A)
- Radical formation is not dependent on the presence of TRX, as it is seen in EDFS measurements of the free photoexcitable labels as well (Figure S21 B, shown for RB-MA)

- Three consecutive freeze-pump-thaw cycles do not suppress radical formation; it is not connected to residual oxygen
- The radical is persistent only at cryogenic temperatures and no longer observed upon thawing and refreezing of the sample
- The addition of ascorbate, a reducing agent, to a solution of free photoexcitable label leads to an increase in radical signal intensity (Figure S21 C, shown for AT12-MA) but does not affect the triplet relaxation behaviour significantly (Figure S21 D, compare to Figure S12 C)

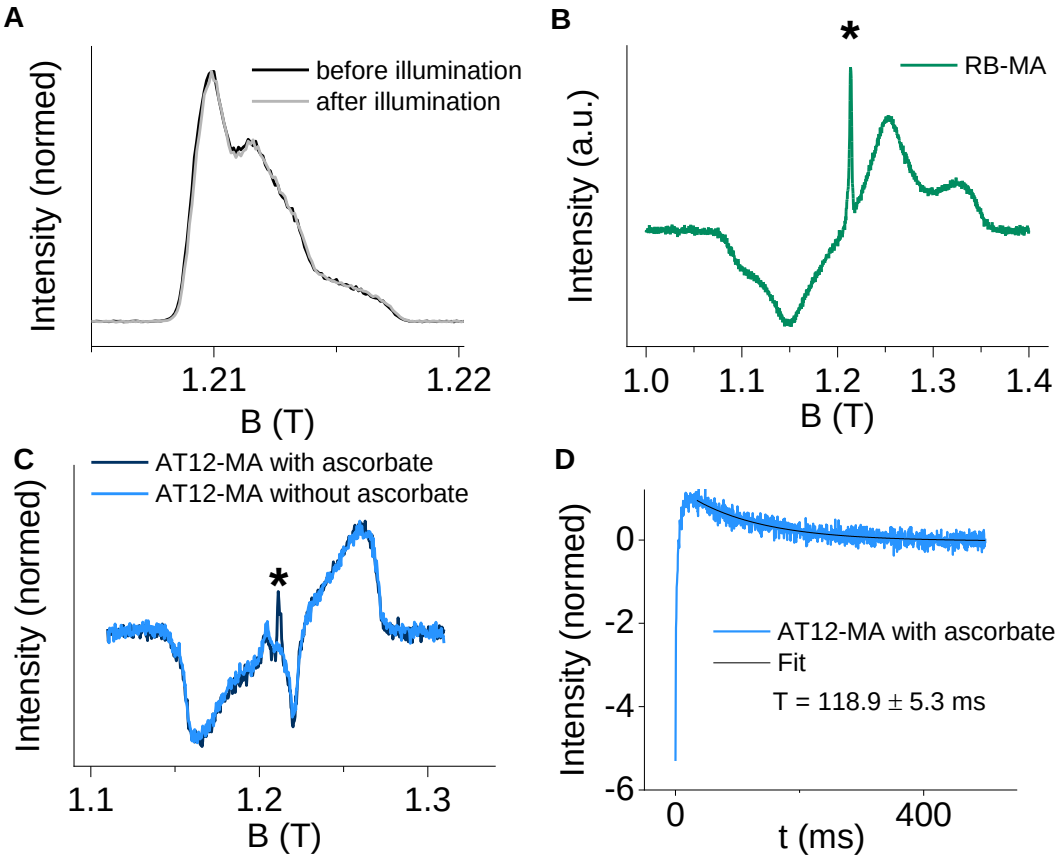

Figure S21. Study of the formation of an illumination-induced persistent radical at 10 K. (A) EDFS spectrum (1 scan) of a solution of 3-maleimido-PROXYL (100 µM) in 60/40 glycerol-d8/D_2O before (black) and after (red) illumination. The sample was subjected to three LaserIMD experiments at 510, 550 and 582 nm in direct succession; the measurement parameters were identical to those chosen for the corresponding LaserIMD experiments on the doubly labelled TRX samples. No persistent radical is observed. (B) EDFS spectrum (sum of 3 scans) of unbound RB-MA (200 µM). The persistent radical is marked with an asterisk. (C) EDFS spectrum (1 scan) of unbound AT12-MA (blue) and unbound AT12-MA in the presence of an 80-fold excess of ascorbate (black, both 50 µM). The persistent radical is marked with an asterisk. (D) Integrated Hahn-echo intensities as a function of the delay after flash of AT12-MA (50 µM) in the presence of an 80-fold excess of ascorbate. The spectrum was collected at the field position corresponding to the emissive transition of the Y canonical orientation of the zero-field splitting (1.22 T). The later part of the decay curve, representing the relaxation of the triplet state, was fitted with a mono-exponential decay function. The obtained T does not differ significantly from the value for AT12-MA without ascorbate (110 ms, see Figure S12C).

Based on these observations and reports in literature on the photochemistry of xanthene dyes, we assume that the radical corresponds to semireduced and semioxidized forms of the photoexcitable

labels. Flash photolysis studies on eosin Y in aqueous solutions showed that these species are formed in an electron dismutation reaction between two triplet molecules in a pathway that competes with the decay of the excited triplet to the singlet ground state; also, the addition of a reducing agent promoted the formation of the semireduced eosin radical.[29] In alcoholic solutions, the semireduced dye appears as an intermediate product in the photoreduction of the dye by the solvent,[30] which is why we do not rule out that the glycerol in the sample may play a role as well. At room temperature, these radicals are transient species that undergo rapid recombination. This would explain why the signal disappears after thawing the sample. We estimate the radical signal to amount to <10 % of the nitroxide signal by the end of the LaserIMD experiment.

To prove that the radicals' presence does not adversely affect the distance determination, we compared the result obtained from analysing only the first scan (during which little to no radical is present) to that of the last scan (maximum radical yield) of the LaserIMD measurement on the TRX_EO-N_3_NO-MA sample (Figure S22). Since neither the dipolar pattern nor the form factor nor the obtained distribution differ noticeably between these scans, we conclude that radical formation can be neglected when extracting distances from the dipolar trace, but might be the reason for the observed photobleaching of the photoexcitable labels.

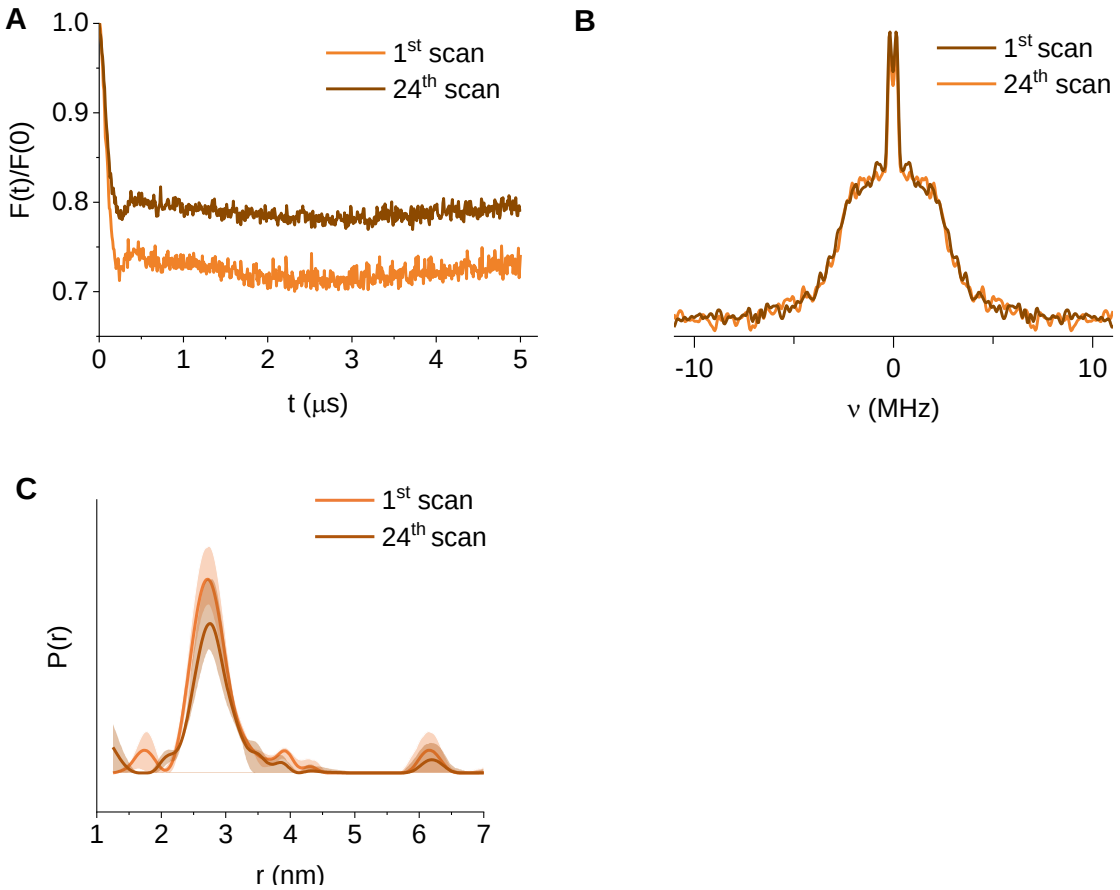

Figure S22. Comparison of the first and last (24th) scan of the LaserIMD experiment performed on TRX labelled with EO-N_3 and NO-MA. (A) Background corrected form factors of the forward parts of the LaserIMD traces. (B) Dipolar spectra obtained by Fourier transformation. (C) Validated distance distribution obtained by Tikhonov regularization. The α parameter was automatically determined by the GCV criterion. No additional distances which could be attributed to the presence of the persistent radical are seen for the 24th scan.

Other influences on modulation depth

If only the first scan of the LaserIMD dataset is considered, the modulation depths for the EO- and RB-labelled samples are below our estimates of 43 – 66 %. One reason might lie in the dependence of Φ_T on solvent and pH, as is evident from the spread of values in literature (e.g., 0.786 in 0.1 mM NaOH[31], 0.98 in 1x PBS pH 7.4[32] and 0.61-0.96[33, 34] in MeOH for RB disodium salt). No data for our 40/60 water/glycerol mixture at 10 K is available, meaning Φ_T could lie below our predictions. Another influence is the efficiency of double labeling. Based on spin, dye and protein concentrations (Table S4) we estimate the degree of double labeling to be between 60 and 90 %; and the presence of cysteine-bridged dimeric TRX after completion of both labeling steps, evidenced by SDS-PAGE gel analysis (Figure S24), confirms a fraction that lacks the cysteine-reactive label. Thus, dimers or monomeric TRX carrying only the nitroxide are addressed by the microwave pulse sequence but not by the laser flash, which results in a modulation depth below the value predicted solely by Φ_T.[8]

Another aspect which deserves attention is the quenching of excited states by nitroxides, a well-documented phenomenon that has been exploited extensively in the design of pro-fluorogenic compounds[35] and could also lead to a reduced modulation depth. To check for this interaction, the influence of the nitroxide spin label on the relaxation of the photoexcitable labels' triplet states in the doubly labelled TRX samples was studied as described under "Triplet relaxation" in section 5.3, i.e. by increasing the delay between laser excitation and a Hahn echo sequence. Since the deactivation of the triplet state of eosin by nitroxides has been reported in literature,[36, 37] we would expect any such effect in our systems to manifest itself in a significantly accelerated triplet signal decay.

To perform these experiments, two types of samples were prepared according to the LaserIMD sample preparation procedure: one containing 50 µM TRX doubly labelled with a nitroxide and a photoexcitable label (EO-N_3, RB-MA or AT-12), and a control sample, taken from the same stock solution, in which the nitroxide was reduced by adding an 80-fold excess of ascorbate (final concentration: 4 mM) and incubating for 1 h at room temperature.[38] These were then subjected to triplet relaxation measurements, the results of which are shown in Figure S23 . We do not see a significant difference between the samples with and without nitroxide, from which we conclude that the nitroxide does not quench the excited triplet state. Additionally, we find that (compared to free fluorophores) attachment to the protein, which could promote deactivation of the excited state,[39] did not significantly change the results.

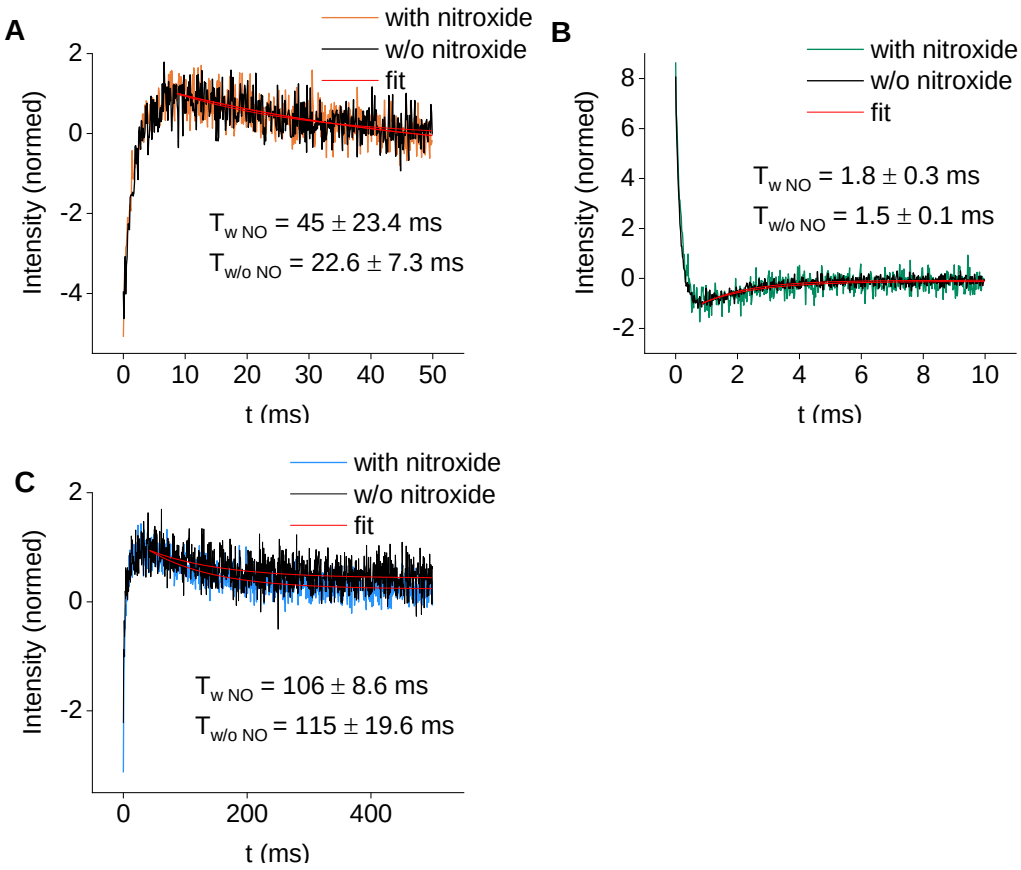

Figure S23. Integrated Hahn-echo intensities as a function of the delay after flash, used to study the influence of the nitroxide spin label on the relaxation of the photoexcitable labels' excited triplet states. The spectra were collected at field positions corresponding to the emissive (EO-N_3, AT12-MA) or absorptive (RB-MA) transition of the Y canonical orientation of the zero-field splitting. The later part of the decay curve, corresponding to the relaxation of the triplet state, was fitted with a mono-exponential decay function. For the measurements with nitroxide (colour), a 50 µM sample of TRX labelled with a nitroxide and a photoexcitable label was used; for the measurements without nitroxide (black), the latter was reduced by addition of an 80-fold excess of ascorbate. (A) Trx_EO-N_3_NO-MA (1.2 T) (B) Trx_RB-MA_NO-N_3 (1.25 T) (C) Trx_AT12-MA_NO-N_3 (1.22 T).

Table S4. Details of LaserIMD and DEER samples and measurement parameters. Concentration of the protein ($c_{protein}$), the nitroxides (c_{Spin}), and the triplet label (c_{dye}) are listed. Changes in the absorption spectra of the dyes after attachment to the protein (Figure S25) and the contribution of the nitroxide spin labels to the absorption at 280 nm may lead to inaccuracies in the photometric protein and dye concentration determination, which explains dye and spin labeling degrees > 100 %. The excitation wavelength for the chromophore (λ), π-pulse length of the observer pulses ($t_{\pi,\ obs}$, rectangular observer pulses for LaserIMD, Gauss pulses for DEER experiments), evolution time (d2), shot repetition time (SRT), the number of scans, shots per point (SPP) and the measurement temperature (T) are given. For LaserIMD measurements, the laser power was between 2 - 5 mJ and the samples were prepared in 60 % d8-glycerol and 40 % D_2O to yield a transparent glass to ensure good light transmission for optical excitation. DEER samples contained 20 % d8-glycerol and 80 % D_2O. The π pump pulse for both DEER traces was a 100 ns long, 90 MHz broad HS[1] pulse ($\beta/t_p = 8$) that was set to the nitroxide and resonator maximum with an offset of +90 MHz to the observer pulses.

Sample	TRX_EO-N_3 _NO-MA	TRX_EO-MA _NO-N_3	TRX_RB-MA _NO-N_3	TRX_AT12-MA _NO-N_3	TRX_NO-MA_ NO-MA	TRX_NO-N_3 _NO-N_3
$c_{protein}$ (µM)	115	72	100	47	45	142
c_{Spin} (µM)	106	48	50	56	137	238
c_{Dye} (µM)	110	77	90	67	-	-
λ (nm)	510	510	550	582	-	-
$t_{\pi,\ obs}$ (ns)	8	8	8	10	64	60
d2 (µs)	5000	4000	5000	5000	8000	8000
SRT (ms)	60	60	50	1000	4,05	4,05
scans	24	12	24	24	70	70
SPP	1	2	1	1	1	1
T (K)	10	10	10	10	50	50

7. Characterization of doubly labelled TRX

7.1 SDS PAGE

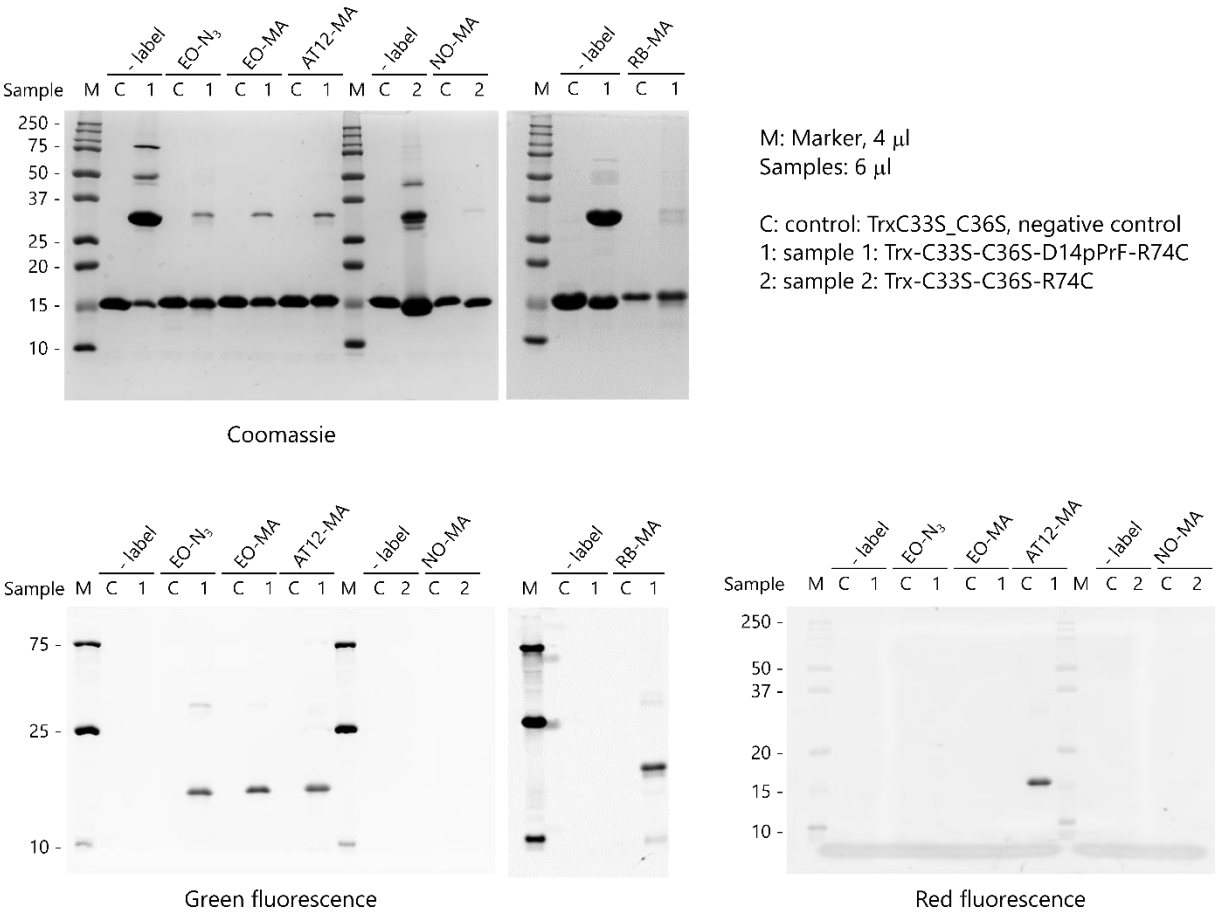

Figure S24. SDS-PAGE of double labeling of TRX at positions 14 (CuCAAC reaction) and 74 (Cys-Maleimide coupling) with one fluorescent dye at one site and one spin label at the other. (A) 15 % SDS-PAGE stained with Coomassie brilliant blue, showing protein bands before (-label) and after labeling reaction with the different labels. (B) The same (unstained) gel illuminated with 520 nm showing green fluorescence for Eosin-, RB- and AT12-labelled proteins, but not for the respective controls, while illumination with 630 nm (red fluorescence) shows AT12 only.

7.2 UV-Vis Spectra

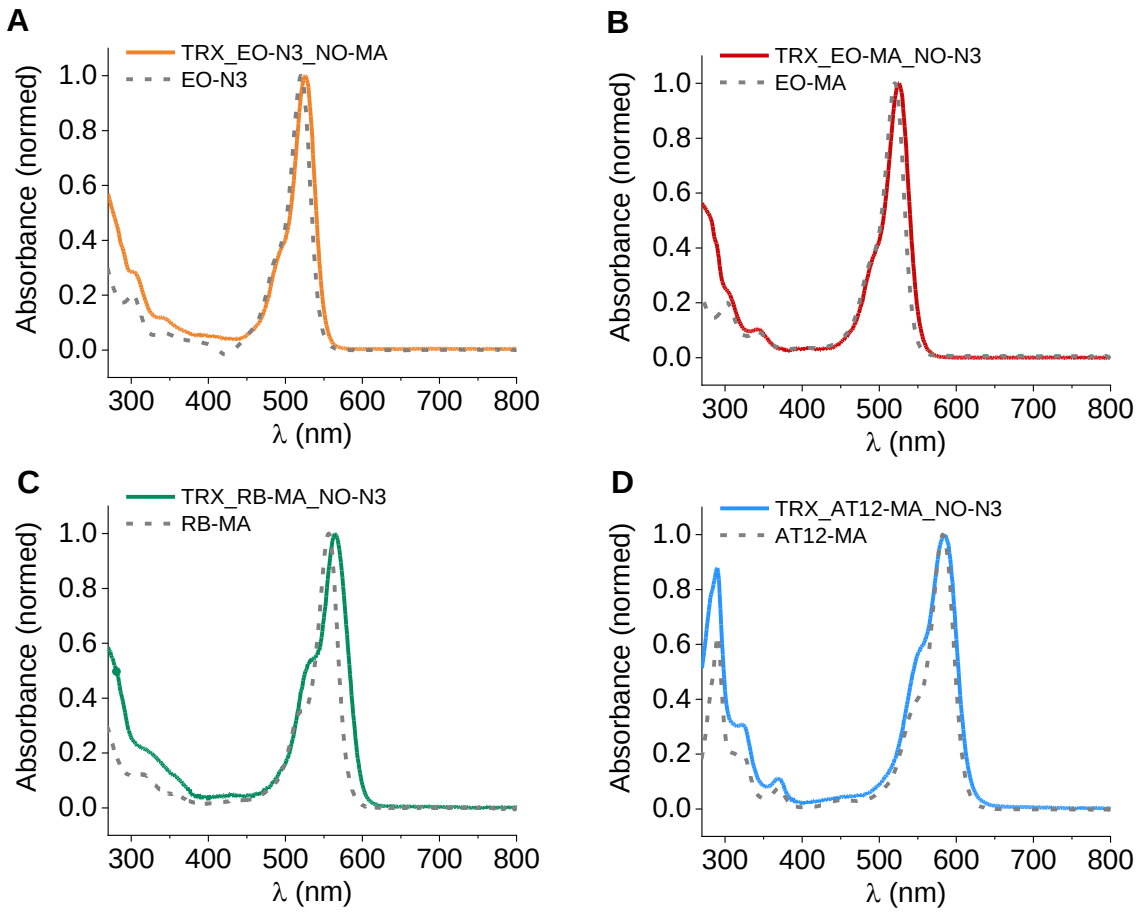

Figure S25. Normalized UV-Vis spectra in deionized water of TRX labeled at positions 14 (CuCAAC reaction) and 74 (Cys-Maleimide coupling) with: (A) EO-N_3/NO-MA (orange). (B) EO-MA/NO-N_3 (red). (C) RB-MA/NO-N_3 (green). (D) AT12-MA/NO-N_3 (blue). Spectra are compared to those of the unbound photoexcitable spin labels in deionized water (grey dashed lines). The increase in absorbance at 280 nm indicates successful attachment to TRX.

7.3 Circular Dichroism (CD)

Protein samples were diluted to 20 µM in deionized water and 100 µL were transferred to 0.5 mm demountable cuvettes. Spectra were recorded on a JASCO J-715 spectropolarimeter by continuously scanning from 280 to 180 nm with a scanning speed of 50 nm/min, response time of 4 s and a bandwidth of 1.0 nm at 20 °C. The recorded spectra were averaged over 10 scans, baseline-corrected and background-corrected with deionized water. For the conversion of the spectrometer unit (CD-signal in mdeg) to the molar residue ellipticity (MRE), the formula MRE = [MRW*CD-signal/1000]/(10*d*c) with M in g/mol, N_{aa} as the number of amino acid residues in the protein, MRW = M/N_{aa}, c in g/mL, and d = 0.05 cm, was used (Figure S26).

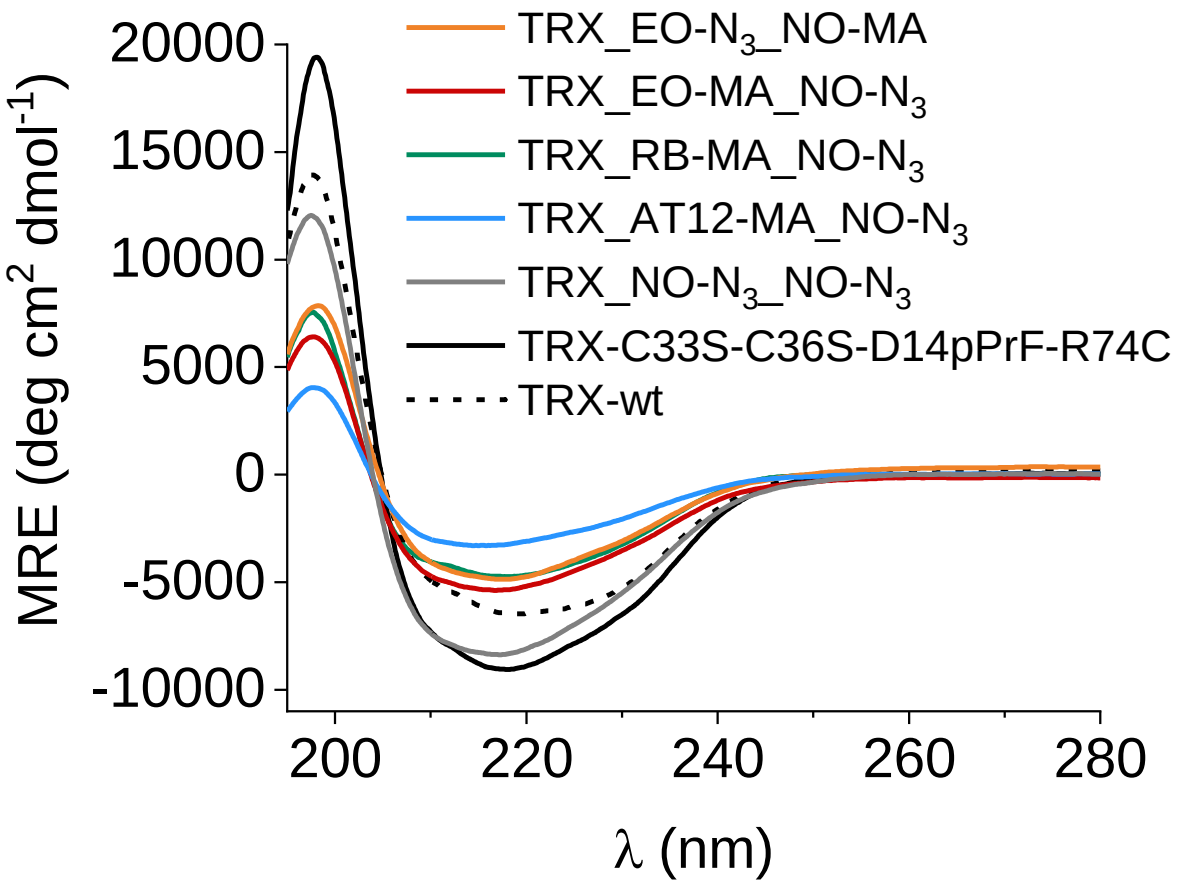

Figure S26. CD spectra in deionized water of TRX wild-type (wt, dashed line), the unlabeled TRX mutant (black), TRX doubly labeled with a photoexcitable spin label and a nitroxide label (color) and TRX doubly labelled with NO-N_3 (grey). CD spectra of TRX wt and the unlabeled TRX mutant are compared to TRX doubly labeled with NO-N_3 (grey), with EO-N_3 and NO-MA (orange), with EO-MA and NO-N_3 (red), with AT12-MA and NO-N_3 (blue) and with RB-MA and NO-N_3 (green). Spectra are normalized to mean residue ellipticity (MRE). No qualitative change to the spectral shape is observed upon labeling. Quantitative deviations are attributed to inaccuracies in the photometric protein concentration determination, which arise from changes in the absorption spectra of the dyes after attachment to the protein (Figure S25), and the contribution of the nitroxide spin labels to the absorption at 280 nm.

7.4 Protein mass spectrometry

All samples were purified by UHPLC on a Dionex UltiMate3000 (Thermo Fisher Scientific, Germany) using an analytical Aeris WIDEPORE XB-C8 column (150 mm x 2.1 mm) with 3.6 µm silica as a stationary phase (Phenomenex, Germany). Prior to purification, all samples were acidified with 0.1% TFA. Gradient elution (5 min at 0% B; in 30 min to 70% B; then in 15 min to 100% B) with eluent A (0.04% TFA in water) and eluent B (0.04% TFA in acetonitrile/water (80:20, v/v)) was performed at a flow rate of 250 µl/min. The signals were monitored by UV absorbance at 220 nm. Intact proteins were analysed by direct infusion on an amazon speed ETD mass spectrometer (Bruker Daltonics) with a flow rate of 4 µl/min. The mass spectrometric data were acquired for about 7 minutes and the final mass spectrum was averaged over the whole acquisition time. Mass spectrometric data were evaluated and deconvoluted using the Compass Data Analysis Version 4.4 (Bruker Daltonics) software.

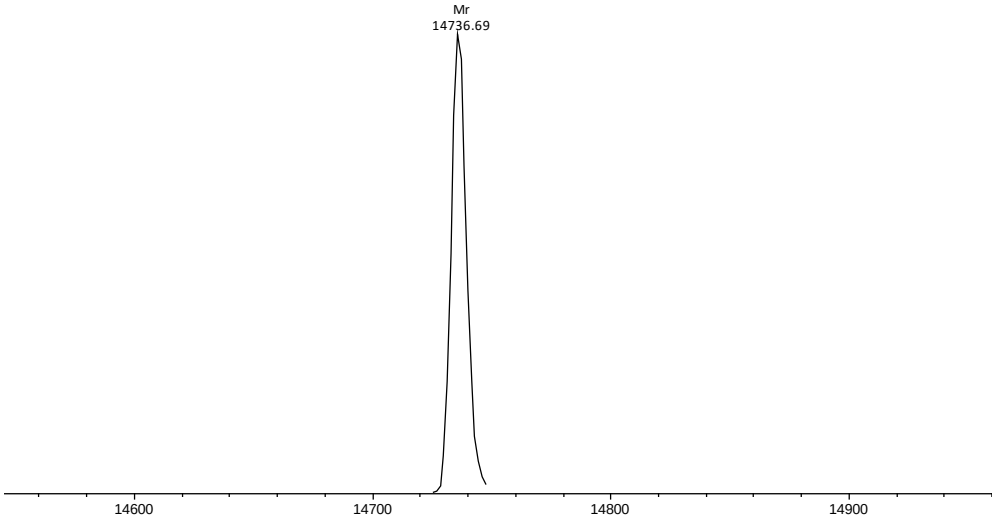

Figure S27. Full-length ESI-MS spectra of TRX_C33S_C36S (control) after protein expression and purification. Found and calculated masses are shown in the following table. The mass difference of 158 Da corresponds to the loss of formyl-methionine (fMet) due to partial editing.[40]

Sample	Found m/z	Calculated m/z	Assignment
C33S/C36S TRX	14737	14736 (14927 Da (wt TRX)[19] – 158 Da (fMet) – 2*121 Da (C) + 2*105 Da (S))	C33S/C36S TRX – fMet

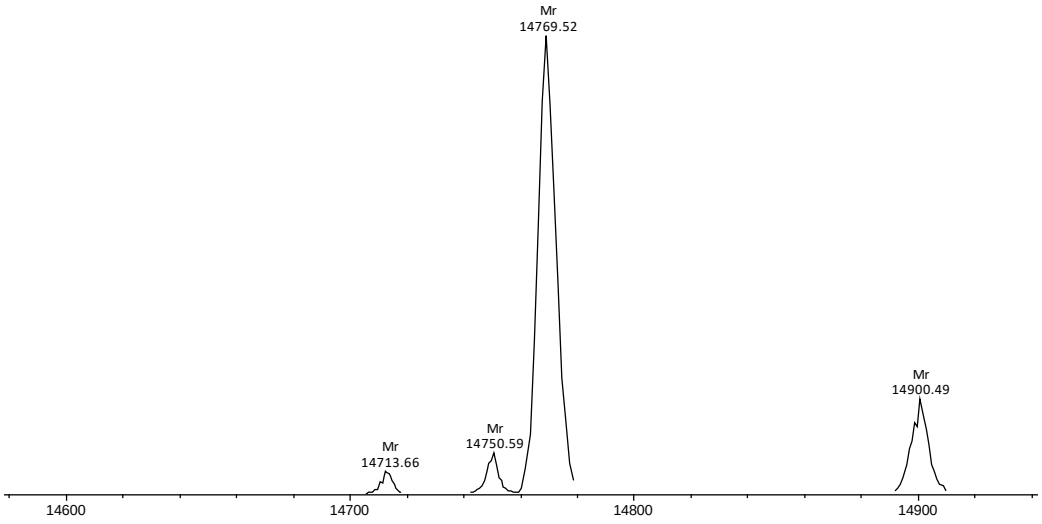

Figure S28. Full-length ESI-MS spectra of TRX_C33S_C36S_D14pPrF_R74C after protein expression and purification. Found and calculated masses are shown in the following table.

Sample	Found m/z	Calculated m/z	Assignment
C33S/C36S/D14pPrF/R74C TRX after expression	14770	14769 (14736 Da – 133 Da (D) – 174 Da (R) + 121 Da (C) + 219 Da (pPrF))	C33S/C36S/D14C/R74pPrF TRX – fMet

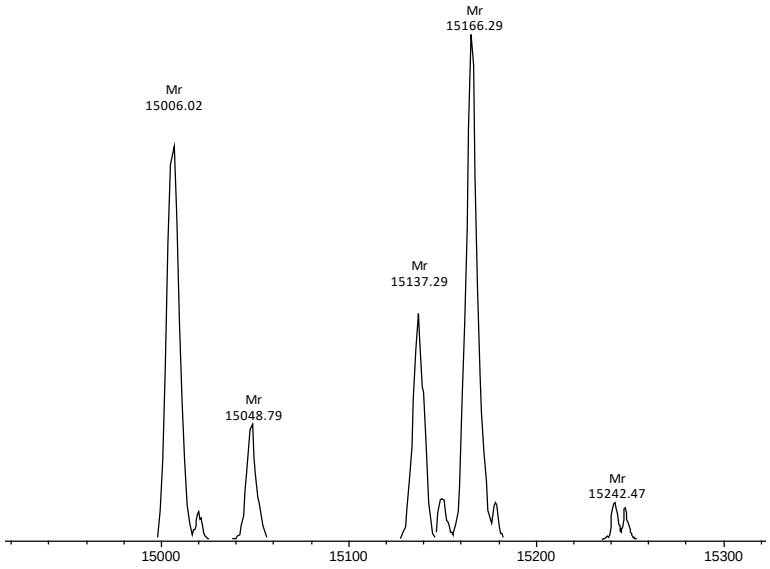

Figure S29. Full-length ESI-MS spectra of TRX_C33S_C36S_D14C_R74C after protein expression, purification and labeling with NO-MA. Found and calculated masses are shown in the following table.

Sample	Found m/z	Calculated m/z	Assignment
C33S/C36S/D14C/R74C TRX after labeling	15137	15145 (14736 Da - 133 Da (D) – 174 Da (R) + 2*121 Da (C) + 2*237 Da (NO-MA)))	doubly labelled C33S/C36S/D14C/R74C TRX - fMet
	15166	= 15146 Da + 20 Da (NH_4)	

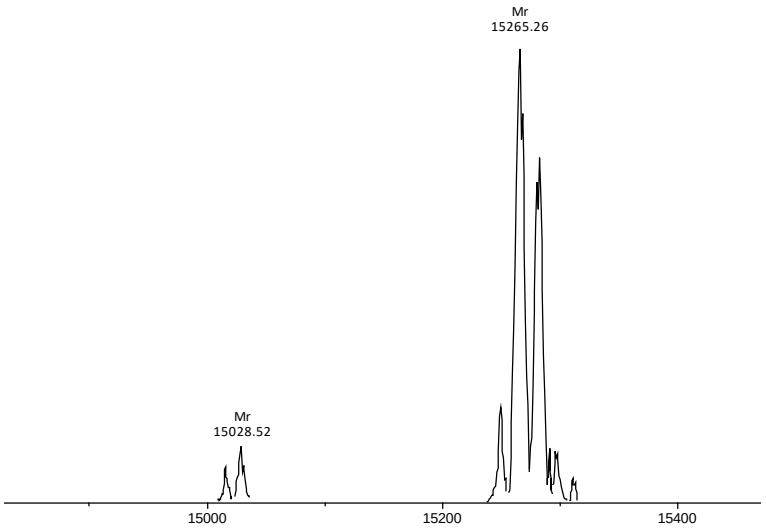

Figure S30. Full-length ESI-MS spectra of TRX_C33S_C36S_D14pPrF_R74pPrF after protein expression, purification and after labeling with NO-N_3. Found and calculated masses are shown in the following table.

Sample	Found m/z	Calculated m/z	Assignment
C33S/C36S/D14pPrF/R74pPrf TRX	15265	15262 (14736 Da – 133 Da (D) - 174 Da (R) + 2*219 Da (pPrF) + 2*197 Da (NO-N_3))	Doubly labeled C33S/C36S/D14pPrF/R74pPrf TRX – fMet

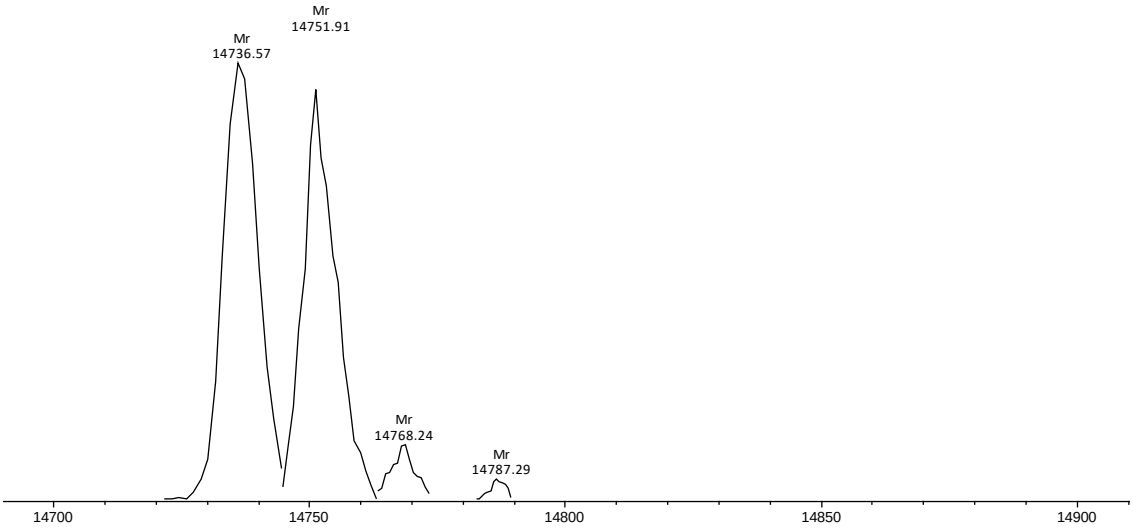

Figure S31. Full-length ESI-MS spectra of TRX_C33S_C36S after protein expression, purification and labeling with EO-N_3 and NO-MA. Found and calculated masses are shown in the following table. The mass increment of 17 Da between the two peaks is believed to stem from an oxygen adduct from photooxidation by the dye.

Sample	Found m/z	Calculated m/z	Assignment
C33S/C36S TRX	14737	14736	Unlabeled C33S/C36S TRX – fMet
	14752	14752 (14736 Da + 16 Da (0.5 O_2))	

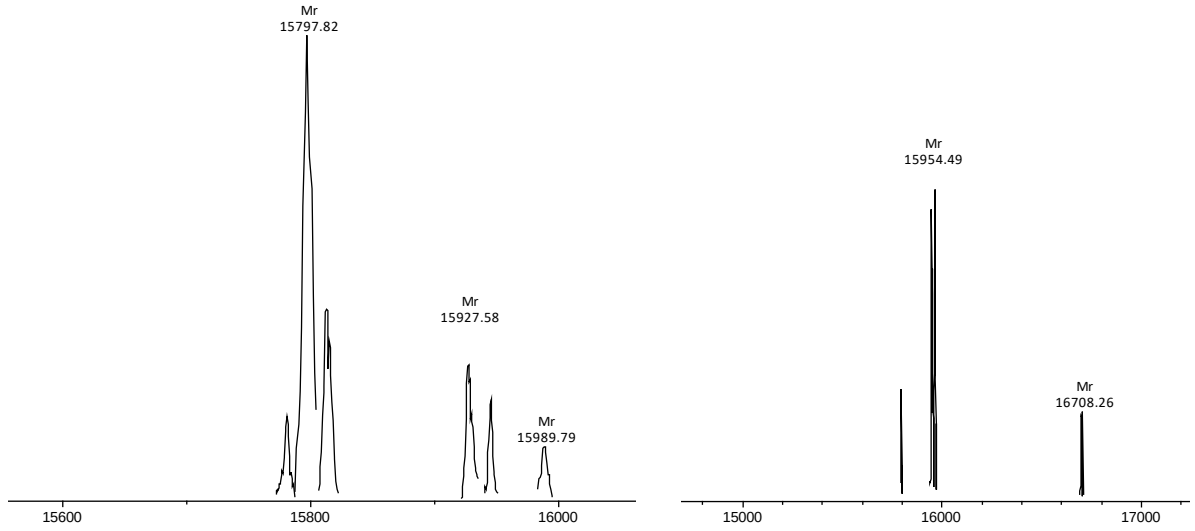

Figure S32. ESI-MS spectra of TRX_C33S_C36S_D14pPrF_R74C after protein expression, purification and labeling with EO-N_3 and NO-MA. Found and calculated masses are shown in the following table.

Sample	Found m/z	Calculated m/z	Assignment
C33S/C36S/D14pPrF/R74C TRX after labeling	15798	15797 (14770 Da + 791 Da (EO-N_3) + 237 Da (NO-MA))	Doubly labeled C33S/C36S/D14pPrF/R74C TRX – fMet
	15954	15956 (14770 Da + 158 Da (fMet) + 791 Da (EO-N_3) + 237 Da (NO-MA))	Doubly labeled C33S/C36S/D14pPrF/R74 TRX

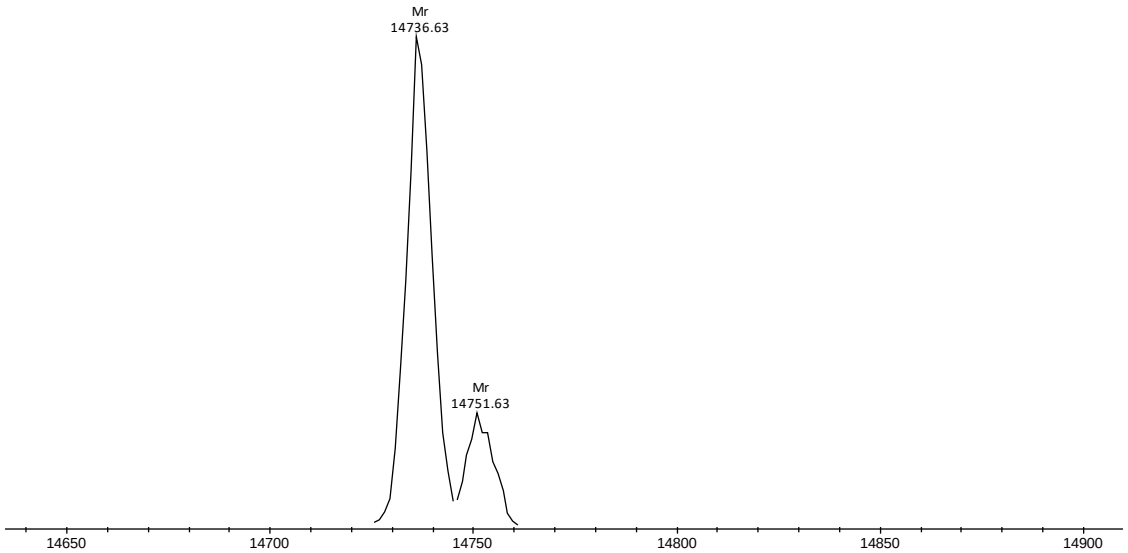

Figure S33. Full-length ESI-MS spectra of TRX_C33S_C36S after protein expression, purification and labeling with EO-MA and NO-N_3. Found and calculated masses are shown in the following table. The mass increment of 15 Da between the two peaks is believed to stem from an oxygen adduct from photooxidation by the dye.

Sample	Found m/z	Calculated m/z	Assignment
C33S/C36S TRX after labeling	14737	14736	Unlabeled C33S/C36S TRX - fMet
	14752	14752 (14736 Da + 16 Da (0.5 O_2))	

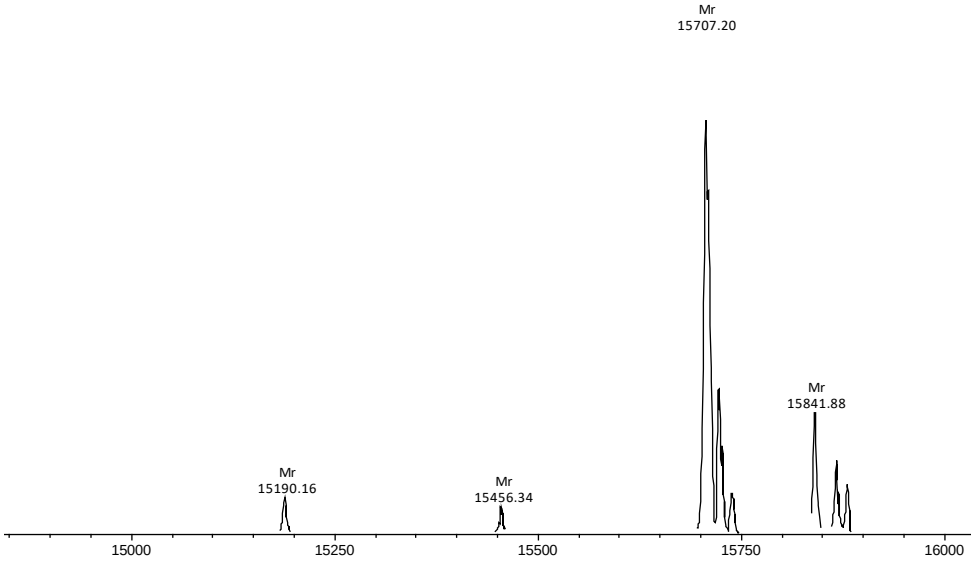

Figure S34. ESI-MS spectra of TRX_C33S_C36S_D14pPrF_R74C after protein expression, purification and labeling with EO-MA and NO-N_3. Found and calculated masses are shown in the following table.

Sample	Found m/z	Calculated m/z	Assignment
C33S/C36S/D14pPrf/R74C TRX after labeling	15707	15710 (14770 Da + 743 Da (EO-MA) + 197 Da (NO-N_3))	Doubly labeled C33S/C36S/D14pPrf/R74C TRX - fMet

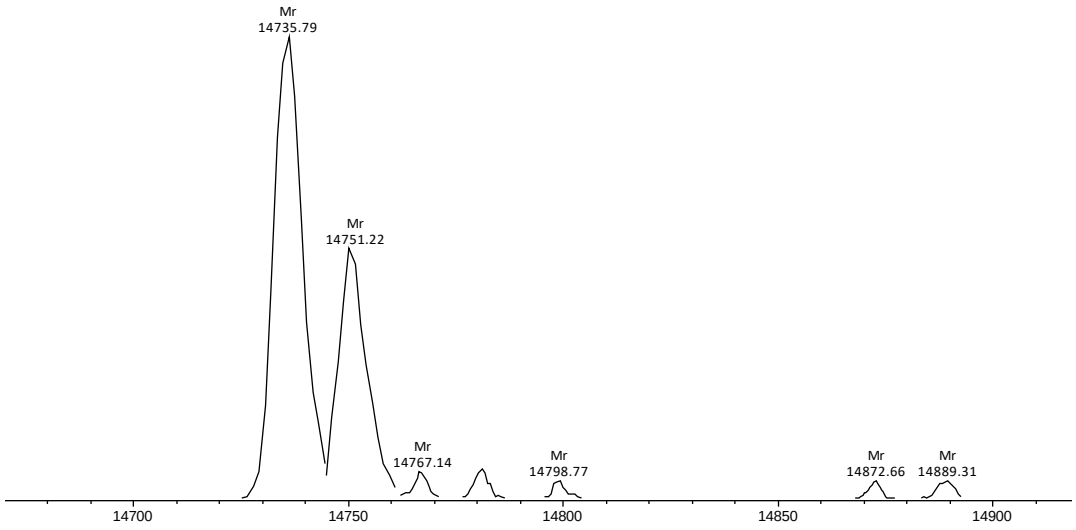

Figure S35. Full-length ESI-MS spectra of TRX_C33S_C36S after protein expression, purification and labeling with RB-MA and NO-N3. Found and calculated masses are shown in the following table. The mass increment of 15 Da between peaks is believed to stem from an oxygen adduct from photooxidation by the dye.

Sample	Found m/z	Calculated m/z	Assignment
C33S/C36S TRX after labeling	14736	14736	Unlabeled C33S/C36S TRX - fMet
	14751	14752 (14736 Da + 16 Da (0.5 O_2))	

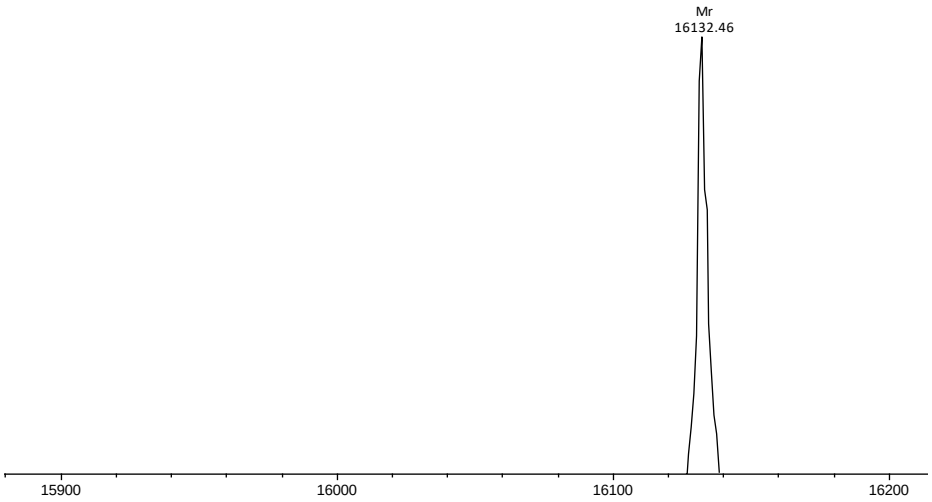

Figure S36. Full-length ESI-MS spectra of TRX_C33S_C36S_D14pPrF_R74C after protein expression, purification and labeling with RB-MA and NO-N_3. Found and calculated masses are shown in the following table.

Sample	Found m/z	Calculated m/z	Assignment
C33S/C36S/D14pPrf/R74C TRX after labeling	16132	16135 (14770 Da + 1168 Da (RB-MA) +197 Da (NO-N_3)	Doubly labeled C33S/C36S/D14pPrf/R74C TRX -fMet

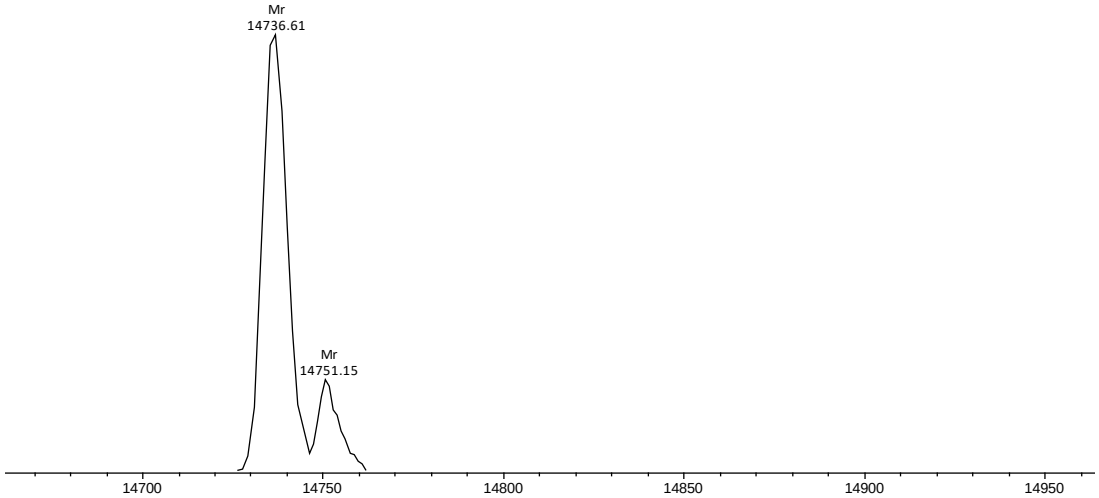

Figure S37. ESI-MS spectra of TRX_C33S_C36S after protein expression, purification and labeling with AT12-MA and NO-N_3. The mass increment of 14 Da between the two peaks is believed to stem from an oxygen adduct from photooxidation by the dye. Found and calculated masses are shown in the following table.

Sample	Found m/z	Calculated m/z	Assignment
C33S/C36S TRX after labeling	14737	14736	C33S/C36S TRX -fMet
	14751	14753 (14736 Da + 16 Da (0.5 O_2))	

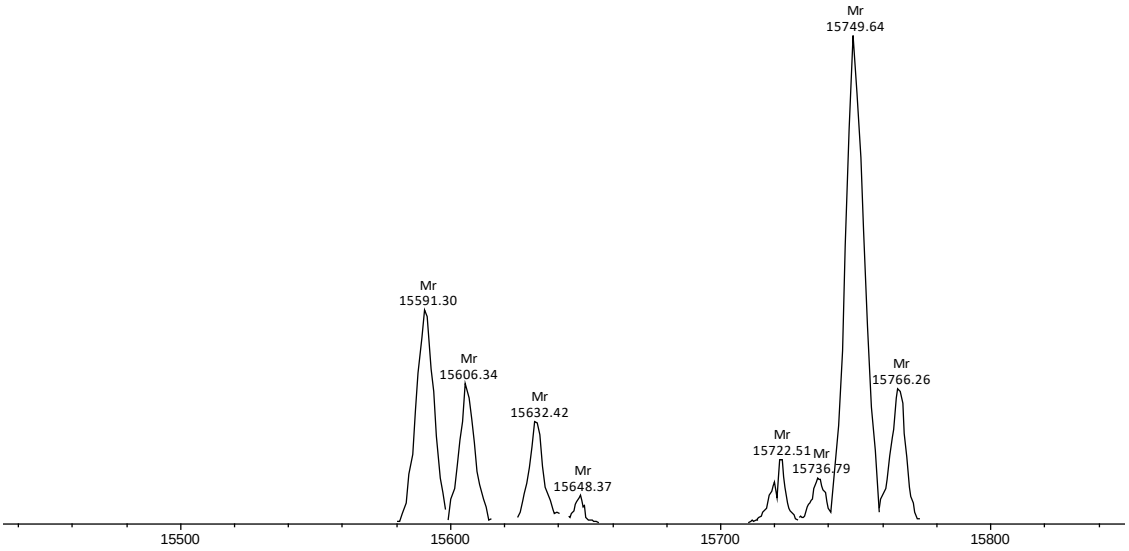

Figure S38. ESI-MS spectra of TRX_C33S_C36S_D14pPrF_R74C after protein expression, purification and labeling with AT12-MA and NO-N_3. Found and calculated masses are shown in the following table. Mass increments of 15 and 16 Da between peaks are believed to stem from oxygen adducts from photooxidation by the dye.

Sample	Found m/z	Calculated m/z	Assignment
C33S/C36S/D14pPrf/R74C TRX	15589	15591 (14770 Da + 624 Da (AT12-MA) +197 Da (NO-N_3))	Doubly labeled C33S/C36S/D14pPrf/R74C TRX - fMet
	15606	15607 (15589 Da + 16 Da (0.5 O_2))	
	15749	15749 (14770 Da +158 (fMet) + 624 Da (AT12-MA) +197 Da (NO-N3))	Doubly labeled C33S/C36S/D14pPrf/R74C TRX
	15766	15765 (15749 Da + 16 Da (0.5 O_2))	

8. References

1. F. J. M. v. d. Ven and 1953-, 1995.
2. P. Schöps, P. E. Spindler, A. Marko and T. F. Prisner, *J. Magn. Reson.*, 2015, **250**, 55-62.
3. C. R. Timmel, C. E. Fursman, A. J. Hoff and P. J. Hore, *Chem. Phys.*, 1998, **226**, 271-283.
4. V. Blechta and J. Schraml, *Journal of Magnetic Resonance (1969)*, 1986, **69**, 293-301.
5. D. G. Donne and D. G. Gorenstein, *Concepts in Magnetic Resonance*, 1997, **9**, 95-111.
6. K. M. Salikhov, S. G. Zech and D. Stehlik, *Mol. Phys.*, 2002, **100**, 1311-1321.
7. M. G. Dal Farra, S. Ciuti, M. Gobbo, D. Carbonera and M. Di Valentin, *Mol. Phys.*, 2019, **117**, 2673-2687.
8. C. Hintze, D. Bücker, S. Domingo Köhler, G. Jeschke and M. Drescher, *J. Phys. Chem. Lett.*, 2016, **7**, 2204-2209.
9. N. J. Turro, M. H. Kleinman and E. Karatekin, *Angew. Chem. Int. Ed.*, 2000, **39**, 4436-4461.
10. J. A. Weil, J. R. Bolton and J. E. Wertz, *New York*, 1994.
11. J. Telser, *eMagRes*, 2007, 207-234.
12. M. E. Rose, *Elementary theory of angular momentum*, Courier Corporation, 1995.
13. S. Steigmiller, M. Börsch, P. Gräber and M. Huber, *Biochimica et Biophysica Acta (BBA)-Bioenergetics*, 2005, **1708**, 143-153.
14. E. Bordignon, *EMagRes*, 2007, 235-254.
15. M. Di Valentin, M. Albertini, E. Zurlo, M. Gobbo and D. Carbonera, *J. Am. Chem. Soc.*, 2014, **136**, 6582-6585.
16. S. J. Welsch, M. Umkehrer, C. Kalinski, G. Ross, C. Burdack, J. Kolb, M. Wild, A. Ehrlich and L. A. Wessjohann, *Tetrahedron Lett.*, 2015, **56**, 1025-1029.
17. C. Fowley, N. Nomikou, A. P. McHale, P. A. McCarron, B. McCaughan and J. F. Callan, *J. Mater. Chem.*, 2012, **22**.
18. S. Kucher, S. Korneev, S. Tyagi, R. Apfelbaum, D. Grohmann, E. A. Lemke, J. P. Klare, H.-J. Steinhoff and D. Klose, *J. Magn. Reson.*, 2017, **275**, 38-45.
19. P. Widder, F. Berner, D. Summerer and M. Drescher, *ACS Chem. Biol.*, 2019, **14**, 839-844.
20. N. Barbero, C. Barolo and G. Viscardi, *World Journal of Chemical Education*, 2016, **4**, 80-85.
21. A. Doll and G. Jeschke, *J. Magn. Reson.*, 2014, **246**, 18-26.
22. G. Jeschke and Y. Polyhach, *PCCP*, 2007, **9**, 1895-1910.
23. C. E. Tait and S. Stoll, *PCCP*, 2016, **18**, 18470-18485.
24. S. Stoll and A. Schweiger, *J. Magn. Reson.*, 2006, **178**, 42-55.
25. G. Jeschke, V. Chechik, P. Ionita, A. Godt, H. Zimmermann, J. Banham, C. Timmel, D. Hilger and H. Jung, *Appl. Magn. Reson.*, 2006, **30**, 473-498.
26. K. Serrer, C. Matt, M. Sokolov, S. Kacprzak, E. Schleicher and S. Weber, *Mol. Phys.*, 2019, **117**, 2688-2699.
27. G. Jeschke, *Annu. Rev. Phys. Chem.*, 2012, **63**, 419-446.
28. L. Song, C. Varma, J. Verhoeven and H. J. Tanke, *Biophys. J.*, 1996, **70**, 2959.
29. V. Kasche and L. Lindqvist, *Photochem. Photobiol.*, 1965, **4**, 923-933.
30. K. Uchida, S. Kato and M. Koizumi, *Nature*, 1959, **184**, 1620-1621.
31. A. Penzkofer, M. Simmel and D. Riedl, *J. Lumin.*, 2012, **132**, 1055-1062.
32. O. Berndt, F. Bandt, I. Eichwurzel and H. Stiel, *Acta Physica Polonica Series A*, 1999, **95**, 207-220.
33. S. Reindl and A. Penzkofer, *Chem. Phys.*, 1996, **213**, 429-438.
34. P. Murasecco-Suardi, E. Gassmann, A. M. Braun and E. Oliveros, *Helv. Chim. Acta*, 1987, **70**, 1760-1773.
35. J. P. Blinco, K. E. Fairfull-Smith, B. J. Morrow and S. E. Bottle, *Australian Journal of Chemistry*, **4**, 373 –389.
36. H. Koloczek and J. M. Vanderkooi, *Biochim. Biophys. Acta*, 1987, **916**, 236-244.

37. Y. YUDANOVA, V. MECKLER, V. FOGEL, A. KULIKOV, A. KOTELNIKOV, G. LIKHTENSTEIN, M. BERKOVICH, A. KARYAKIN, A. ARCHAKOV and A. KAPLUN, *Eur. J. Biochem.*, 1986, **156**, 541-544.
38. S. Bleicken, T. E. Assafa, H. Zhang, C. Elsner, I. Ritsch, M. Pink, S. Rajca, G. Jeschke, A. Rajca and E. Bordignon, *ChemistryOpen*, 2019, **8**, 1057-1065.
39. G. J. Fisher, C. Lewis and D. Madill, *Photochem. Photobiol.*, 1976, **24**, 223-228.
40. M. J. Schmidt and D. Summerer, *Angew. Chem. Int. Ed.*, 2013, **52**, 4690-4693.